

# EveNet: A Foundation Model for Particle Collision Data Analysis

Ting-Hsiang Hsu<sup>1</sup>, Bai-Hong Zhou<sup>2</sup>, Qibin Liu<sup>3</sup>, Yue Xu<sup>4</sup>, Shu Li<sup>2</sup>, George Wei-Shu Hou<sup>1</sup>, Benjamin Nachman<sup>1,5</sup>, Shih-Chieh Hsu<sup>4</sup>, Vinicius Mikuni<sup>6,\*</sup>, Yuan-Tang Chou<sup>4,†</sup> and Yulei Zhang<sup>4,‡</sup>

<sup>1</sup>*Department of Physics, National Taiwan University, Taipei, Taiwan*

<sup>2</sup>*Tsung-Dao Lee Institute, Shanghai Jiao Tong University, Shanghai, China*

<sup>3</sup>*Fundamental Physics Directorate, SLAC National Accelerator Laboratory, Menlo Park, USA*

<sup>4</sup>*Department of Physics, University of Washington, Seattle, Washington, USA*

<sup>5</sup>*Department of Particle Physics and Astrophysics, Stanford University, Stanford, USA*

<sup>6</sup>*Kobayashi-Maskawa Institute, Nagoya University, Nagoya, Japan*

(Dated: January 27, 2026)

While deep learning is transforming data analysis in high-energy physics, computational challenges limit its potential. We address these challenges in the context of collider physics by introducing EveNet, an event-level foundation model pretrained on 500 million simulated collision events using a hybrid objective of self-supervised learning and physics-informed supervision. By leveraging a shared particle-cloud representation, EveNet outperforms state-of-the-art baselines across diverse tasks, including searches for heavy resonances and exotic Higgs decays, and demonstrates exceptional data efficiency in low-statistics regimes. Crucially, we validate the transferability of the model to experimental data by rediscovering the  $\Upsilon$  meson in CMS Open Data and show its capacity for precision physics through the robust extraction of quantum correlation observables stable against systematic uncertainties. These results indicate that EveNet can successfully encode the fundamental physical structure of particle interactions, which offers a unified and resource-efficient framework to accelerate discovery at current and future colliders.

## I. INTRODUCTION

Modern collider experiments probe the fundamental laws of nature by analysing petabytes of collision data in the context of a vast and expanding theory space. General particle accelerators such as the Large Hadron Collider (LHC) collide protons at very high energies with the goal of identifying and characterising the wide range of possible new particles produced through particle collisions. Extracting physics requires hundreds of targeted analyses that interpret the measurements through different lenses. Given a targeted physics process, analysts will then optimise their measurement strategy to maximise the sensitivity of the physics process under scrutiny. Machine learning (ML) has been revolutionising the way physics analysis is carried out at the LHC. The ability to extract relevant information from high-dimensional datasets, coupled with the increasing volume of data collected in experiments, has led to the development of several ML models [1]. Some of these methods are general and can be used for multiple physics analyses, such as object identification [2–4]. However, given the specificity of each physics process, the common practice is to train multiple ML models to address specific tasks, such as reconstruction [5] or identification [6] of particles, and to separate signals from background processes [7, 8].

In recent years, foundation models, trained across diverse physics simulations, have demonstrated significant

potential to enhance a wide range of object-level tasks in collider physics, including jet (collimated spray of particles) tagging, anomaly detection, and unfolding [9–14]. Promising results have already been achieved in jet physics and object reconstruction [15–17]. However, genuinely event-level foundation models that simultaneously boost multiple high-level analyses across diverse final states, the cornerstone of modern high energy physics (HEP) measurements, remain largely unexplored. Existing approaches are typically limited to a few downstream tasks [18], narrow physics process coverage [19], or lack validation on collision data [20]. A systematic strategy for pretraining a versatile foundation model on highly diverse simulations and for quantifying its impact on final physics sensitivity in simulations and collision data requires further studies.

Here, we introduce EVENET, a foundation model built upon a point-edge transformer (PET) encoder [13] that serves as the backbone for learning the internal structure of irregular, unordered point clouds from reconstructed collider events (Fig. 1). Each collider event arises from an underlying scattering process followed by particle decays constrained by quantum numbers and conservation laws, giving rise to a hierarchical organisation of the final state through interactions, resonances, and invisible degrees of freedom. The event-level representation in EVENET is designed to reflect this underlying physical structure and to serve as a single unified representation that supports a broad range of standard event-level analysis tasks in collider physics. A central design principle of EVENET is to optimise these diverse tasks coherently in a single latent space through two key mechanisms: shared parameterisation over diffusion time [13] and particle-level denoising-based inpainting of masked or undetectable ob-

\* [vmikuni@hepl.phys.nagoya-u.ac.jp](mailto:vmikuni@hepl.phys.nagoya-u.ac.jp)

† [yuan-tang.chou@cern.ch](mailto:yuan-tang.chou@cern.ch)

‡ [yulei.zhang@cern.ch](mailto:yulei.zhang@cern.ch)

jects. This aligns discriminative and generative tasks within a single latent geometry, encouraging features that can be reused across tasks while task-specific decoders maintain distinct target objectives.

In this study, we pretrain the foundation model **EVENET** on 500 million Monte Carlo (MC)-simulated events from diverse Standard Model (SM) processes and investigate whether this model can streamline the development of deep-learning-based analyses. Unlike standard foundation models in computer vision or natural language processing that rely primarily on self-supervision [21, 22], we adopted a hybrid pretraining strategy that combines supervised and self-supervised objectives, leveraging the exceptionally rich availability of high-fidelity simulations in HEP.

The model was validated in four distinct analysis settings to assess its versatility and generalizability. First, it was tested in search for a new physics scenario, where it often scans the vast parameter space. Analysis often requires training on and generating hundreds of thousands of datasets to cover the full parameter space (e.g., the mass of new particles), which is impractical and necessitates compromises to reduce computational requirements. Second, the model was evaluated in an *out-of-distribution* new-physics search scenario, where hypothetical particles predicted by a new physics model, as well as dominant backgrounds, are absent from the pre-training dataset and typically have only limited simulated data available for dedicated models. Third, we test on *in-distribution* data to measure quantum correlations in top-quark pair production, where the synergy between assignment and the generation of undetectable objects (such as neutrinos) is critical. Finally, we validated that the foundation model, trained solely on simulated events, retains strong performance on collision data. For this purpose, CMS Open Data were used to rediscover known resonance particles and to compare **EVENET** with state-of-the-art anomaly detection methods [23]. Together, these four tasks exemplify how a single foundation model can be applied to precision measurements, new-physics searches, and anomaly detection in standard high-energy physics analyses.

This work makes the following key contributions: (1) we introduce **EveNet**, which is the event-level foundation model for HEP to unify discriminative and generative objectives in a single physics-informed pretraining framework, enabling transfer across heterogeneous downstream tasks; (2) we provide the first comprehensive evaluation of a foundation model on CMS Open Data, demonstrating robust generalisation from simulation to experimental dataset; (3) we present a systematic ablation study that quantifies the impact of different pretraining strategies and task combinations; and (4) we release a fully pretrained, ready-to-use **EVENET** checkpoint to serve as a powerful and versatile starting point for future HEP analyses.

Through this study, we aim to contribute to an emerging paradigm shift toward foundation-model-based work-

flows in the analysis of collider physics experiments. Our work addresses key shortcomings of current ML approaches, which require large amounts of training data and computing resources for each analysis, thereby enabling analyses to benefit from empirical scaling laws with more data and to achieve optimal performance. We propose that the research community adopt and extend this foundation model paradigm for diverse downstream applications, moving beyond custom models tailored to individual analyses toward a shared, high-performing, and computationally efficient foundation.

## II. METHODS

In this section, we give details on dataset preparation, model architecture, and training setup. We also clarify how the downstream analyses were carried out and formalise the performance metrics used in our studies.

### A. Monte Carlo simulation and Open Data

To generate datasets for both pretraining and downstream studies, we employed large-scale MC simulations covering a broad spectrum of SM processes. Event generation was performed using **MADGRAPH5\_aMC@NLO** [24] to compute fundamental interaction probabilities (matrix elements), while **PYTHIA** [25] modelled the subsequent cascades of quarks and gluons, as well as their transformation into observable particles, a process known as parton showering and hadronisation. The resulting events were processed through a detector simulation using **Delphes** [26] configured with a generic detector setup.

All simulated events correspond to proton–proton collisions at  $\sqrt{s} = 13$  TeV. To ensure high-quality training samples, generator-level filters were applied to suppress low-energy or out-of-acceptance events. Specifically, jets, leptons (electrons or muons), and photons were required to have transverse momenta of at least 10 GeV, and charged leptons were restricted to the central region of the detector by imposing a pseudorapidity requirement of  $|\eta| < 2.5$ , where  $\eta$  represents the angle of a particle relative to the beam pipe. Additional process-specific preselections ensured efficient sampling of relevant event topologies; for example, for quantum chromodynamics (QCD) (strong-interaction) events, we demanded at least two jets with  $p_T > 20$  GeV, and for other processes we required the multiplicities of leptons, jets, and  $b$ -tagged jets to be consistent with the topology of the simulated hard process.

The pretraining stage employed a dataset of approximately 3 billion simulated events spanning a broad range of SM processes, from which about 500 million events were retained after applying preselections. This dataset serves as the foundation model corpus for **EVENET**, enabling the network to learn universal event-level repre-

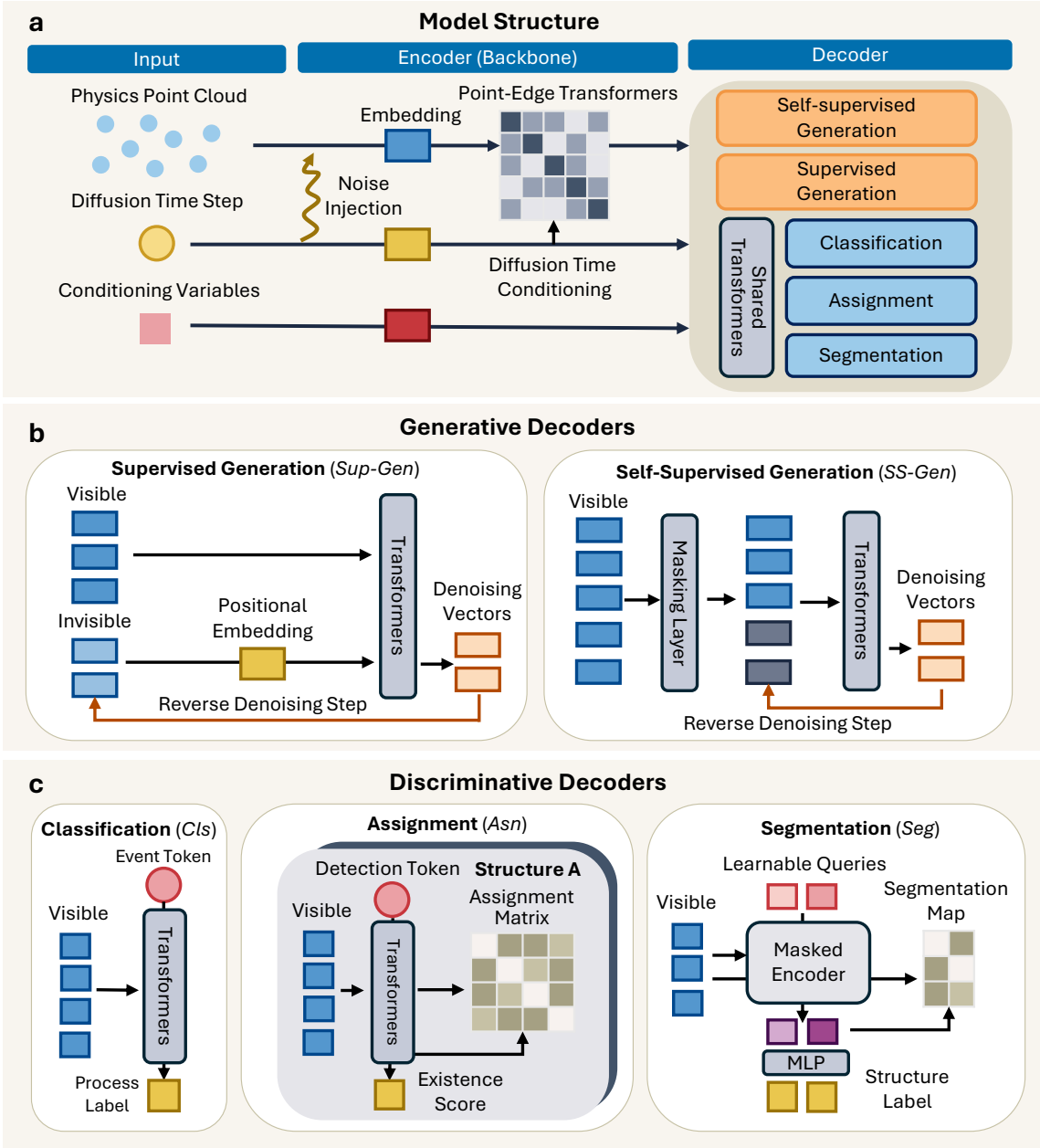


Figure 1: **Overview of the EVENET model architecture and tasks.** (a): Collision events are reconstructed as sets of physics objects and global observables, which form the input to a point–edge transformer encoder. Task-specific decoders extend this shared representation to both generative and discriminative objectives. (b): Self-supervised generation masks a subset of input objects, while supervised generation predicts invisible particles or full event completions using diffusion. (c): Discriminative decoders branch into three task heads aligned with common analysis goals: identifying the physics process (Cls), matching reconstructed objects to their parent resonances (Asn), and grouping objects into final-state categories for event interpretation (Seg).

sentations prior to fine-tuning for downstream analyses. The samples include QCD multijet, top-quark,  $V +$  jets (with  $V = W^\pm, Z$ ), and diboson processes, all processed through the same MC and detector simulation workflow described above.

In addition to the pretraining corpus, four downstream datasets were prepared to evaluate the pretrained model under specific physics analysis settings. (i) For the search for heavy resonance, we utilised the heavy resonance decay to a light scalar and SM Higgs boson ( $X \rightarrow Y H_{SM}$ )

MC simulation from CMS Open Data. (ii) For exotic Higgs-decay searches, we simulated  $H_{\text{SM}} \rightarrow aa$  signal samples for pseudo-scalar mass of  $m_a = 30$  GeV, alongside dominant QCD backgrounds containing two or four  $b$ -jets. (iii) For quantum-correlation studies, we generated  $t\bar{t} \rightarrow 2\ell$  events to probe spin-correlation and entanglement observables in dileptonic top-quark pairs. (iv) For anomaly detection (AD), we used the 2016 CMS Open Data [27] collected at  $\sqrt{s} = 13$  TeV. All simulated processes used for both pretraining and downstream analyses are summarised in Table I.

## B. The algorithm architecture

The Transformer architecture has emerged as a central component of foundation models, owing to its attention mechanism [28] that captures both global dependencies and fine-grained relationships between elements. Its permutation-equivariant structure makes it particularly suitable for representing physics objects in collider experiments. To explicitly model local spatial structure, which encodes essential information about particle interactions in HEP, we augment the Transformer with k-nearest-neighbour networks, resulting in a hybrid point-edge Transformer (PET) architecture [13] that combines global attention with localised geometric awareness. This PET encoder serves as our shared backbone, producing a unified event representation that can be consumed by multiple task-specific heads (Fig. 1).

Reconstructed physics objects, including jets, electrons, and muons, together with their kinematic properties, flavour tagging, lepton identification, and charge information, are represented as point clouds and serve as the model input. A 10% feature dropout rate is applied during pretraining, randomly removing input features for each sample to reduce reliance on specific features and enable more flexible downstream inputs. To accommodate a wide range of analysis needs, our backbone is designed to support both discriminative tasks, such as classification and object pairing, and generative tasks, such as realistic sample generation and the reconstruction of undetectable event components. For the generative objectives, we adopt diffusion models [29], which learn to recover clean events from progressively noised inputs. Conditioning the network on the diffusion time  $t$ , which controls the noise level, provides a single continuum from fully clean events to increasingly perturbed views. The  $t = 0$  endpoint corresponds to the standard discriminative input, whereas  $t > 0$  enables diffusion-based generation. This time-conditioned formulation provides a unified view of the representation space, treating discrimination and generation not as distinct processing modes, but as different points along the same noise trajectory, allowing the same shared backbone to operate consistently across both regimes.

Building on the shared PET backbone, we provide a modular set of task-specific heads for classification, as-

signment, segmentation, supervised and self-supervised generation. These heads can be attached as needed for downstream applications and, when appropriate, incorporated into alternative pretraining recipes. This interface preserves the flexibility of a foundation model, allowing users to plug in custom heads for arbitrary downstream tasks while reusing the same backbone.

The classification head discriminates among underlying physics processes, which is critical for isolating event signatures. During pretraining, the classifier is trained on labels based on event topology, with decay-channel variations absorbed within each class, encouraging the model to learn intrinsic structure rather than exploiting trivial separations based on specific final-state compositions. To further improve robustness during pretraining, we include noise-perturbed examples across the full range of diffusion time steps considered above.

The classification loss is defined in Eq. 1, where  $\alpha(t)$  denotes the time-dependent coefficient from the diffusion process,  $\hat{x}_{\text{perturbed}} = \alpha(t)x + \sigma(t)\epsilon$ , with  $\lim_{t \rightarrow 1} \alpha(t) = 0$  ( $\lim_{t \rightarrow 0} \alpha(t) = 1$ ), where  $x$  and  $\epsilon$  denoting the input and Gaussian noise, respectively. This is used to weight the contributions of examples at different noise levels in the loss.

$$\mathcal{L}_{\text{class}} = \alpha^2(t) \text{CE}(y, \hat{y}_{\text{pred}}) \quad (1)$$

The assignment head maps detector objects to the decay products of the corresponding Feynman diagram, represented as a hierarchical two-tier system of resonances and decay products. For each resonance  $r$ , the assignment matrix encodes the probabilities for assigning the  $n$  point-cloud objects to the  $d_r$  decay products, and has dimensions  $n^{d_r}$ . Multiple Transformer-based heads, each incorporating the Symmetry Tensor Attention framework [6], generate detection probabilities and assignment matrices, encoding the presence of resonances and object-to-decay mappings while respecting intrinsic symmetries among decay products. To better exploit recurring decay topologies and their shared symmetries, we introduce a shared-head scheme in which resonances with identical decay structures are processed by a single head, enabling joint training across multiple diagrams and strengthening the learning of common structural patterns. Physical attributes, such as resonance masses, are provided as conditional inputs to enforce distinguishability while maintaining symmetries among identical resonances. The assignment loss (Eq. 2) averages over physical processes and consists of a permutation-invariant assignment term and a resonance-multiplicity term over unique resonance types. (Here,  $P$  denotes the set of physical processes. For each process  $p \in P$ ,  $R_p$  is the set of resonances and  $G_p$  the symmetry group acting on them. The mask  $\mathcal{M}_r$  identifies non-reconstructable resonances, with  $\text{CB}(\mathcal{M}_r)$  the corresponding class-balance correction.  $\mathcal{P}_r$  and  $\mathcal{T}_r$  are the predicted and target assignment matrices for each resonance  $r$ .  $N_r^{\text{pred}}$  and  $N_r$  are the predicted and target one-hot encoded resonance multiplicities, evaluated over unique resonance types  $R_p^{\text{unique}}$ .

Table I: Summary of generated and selected events used for the pretraining and downstream datasets.

Process	Final States	Generated /M	Sel. Eff. [%]	Used /M
<b>Pretraining Dataset</b>				
QCD	inclusive 2,3,4j	30.4	61.9	18.9
$t\bar{t}$	hadronic / 1L / 2L + 0,1j	422.0	16.6	70.0
$t\bar{t}W$	hadronic / 1L $t\bar{t} + W(\ell\nu)/W(qq')$	692.0	9.0	62.1
$t\bar{t}Z$	hadronic / 1L $t\bar{t} + Z(\ell\ell)/Z(qq)$	630.0	8.9	55.8
$W+jets$	$W(\ell\nu)/W(qq') + 0,1,2j$	121.0	39.9	48.4
$Z+jets$	$Z(\ell\ell)/Z(qq) + 0,1,2j$	129.0	41.2	53.0
$WW$	1L / 2L	262.0	24.8	64.9
$ZZ$	2L / 4L	196.0	18.0	35.3
$WZ$	1L / 2L / 3L	256.0	25.8	66.1
$H_{\text{SM}}(WW^*)$	0L / 1L / 2L	192.0	36.0	69.4
<b>Total</b>	—	2930.4	18.5	543.0
<b>Downstream Datasets</b>				
<i>(i) Resonant <math>X \rightarrow Y H_{\text{SM}}</math> (CMS Open Data)</i>		(train and test = 1:1 split per mass points)		
$X \rightarrow Y H_{\text{SM}} \rightarrow b\bar{b}WW^*$	$b\bar{b} + \ell\nu qq$	$\sim 0.18$ (per mass)	2–11	0.005–0.02
$t\bar{t}$	$b\ell\nu + bqq$	144.7	2.8	4.08
Single top	-	61.54	0.15	0.09
$tW$	-	5.04	0.79	0.04
$Z+heavy$ flavour	$Z(\ell\ell) + b$ jets	9.74	0.62	0.06
<i>(ii) Exotic Higgs Decay <math>H_{\text{SM}} \rightarrow aa</math>, <math>a \rightarrow b\bar{b}</math></i>		(same number for train and test sample)		
QCD		53.47	1.41	0.75
$H_{\text{SM}} \rightarrow aa$		1.25	13.46	0.17
<b>Total</b>		7.25	1.98	0.14
		61.97	1.72	1.06
<i>(iii) Quantum Correlation <math>t\bar{t} \rightarrow 2\ell</math></i>				
Train sample	2L	3.56	12.1	0.43
Test sample	2L	2.40	100.0	2.40
<b>Total</b>	—	5.96	36.1	2.83
<i>(iv) Anomaly Detection (CMS Open Data)</i>				
Channel	Mass window [GeV]	Data points		
Opposite sign		$m_{\mu\mu} \in [5, 9] \cup [10.6, 16]$		
		$m_{\mu\mu} \in [9, 10.6]$		
Same sign		$m_{\mu\mu} \in [5, 9] \cup [10.6, 16]$		
		$m_{\mu\mu} \in [9, 10.6]$		
<b>Total</b>		—		
		10,640		
		1692		
		6179		
		989		
		19,500		

The coefficients  $c_{\text{assign}}$  and  $c_{\text{detect}}$  control the relative con-

tributions of the two terms.)

$$\mathcal{L}_{\text{assignment}} = \frac{1}{N_P} \sum_{p \in P} \left( c_{\text{assign}} \min_{\sigma \in G_P} \sum_{r \in R_p} \frac{\mathcal{M}_{\sigma(r)} \text{CE}(\mathcal{P}_r, \mathcal{T}_{\sigma(r)})}{\text{CB}(\mathcal{M}_{\sigma(r)})} + c_{\text{detect}} \sum_{r \in R_p^{\text{unique}}} \text{CE}(N_r^{\text{pred}}, N_r) \right) \quad (2)$$

The segmentation head reconstructs resonance particles in an object-detection framework, following the end-to-end paradigm of DETR [30] and its mask-based exten-

sions [31]. A set of learnable queries is processed by a Transformer decoder with cross-attention to the encoded point cloud representation and refinement via self-

attention. Each query represents a resonance candidate and is mapped to a segmentation class label and mask, thereby assigning detector objects to the corresponding candidate. This yields a globally consistent interpretation of the event while remaining agnostic to the underlying process. Training employs Hungarian matching [32] to align predictions with targets and preserve permutation symmetry. The matching cost combines classification and mask terms, with mask losses applied only to non-empty targets. Mask supervision uses a weighted

combination of focal [33] and dice losses [34]. The segmentation loss is given by Eq. 3, where  $q \in Q$  indexes decoder queries and  $\hat{o}$  is the optimal Hungarian assignment. The classification term is reweighted by  $w(c_{\hat{o}(q)})$  for class balancing. The mask prediction  $\hat{M}_q^{\text{pred}}$  is supervised with a weighted focal and dice loss and is applied only to non-empty targets via  $\mathbf{1}_{\{c_{\hat{o}(q)} \neq \emptyset\}}$ . The coefficients  $c_{\text{class}}$  and  $c_{\text{mask}}$  set the relative weights of the classification and mask terms.

$$\mathcal{L}_{\text{segmentation}} = \frac{1}{N_P} \sum_{p \in P} \left( \sum_{q \in Q} \left[ c_{\text{class}} w(c_{\hat{o}(q)}) \text{CE} \left( y_{\hat{o}(q)}, \hat{y}_q^{\text{pred}} \right) + c_{\text{mask}} \mathbf{1}_{\{c_{\hat{o}(q)} \neq \emptyset\}} \mathcal{L}_{\text{mask}} \left( M_{\hat{o}(q)}, \hat{M}_q^{\text{pred}} \right) \right] \right), \quad (3)$$

As a self-supervised pretraining objective, the unsupervised generative head is trained using a Transformer-based architecture. A dedicated masking head randomly perturbs a subset of the point cloud and provides a time embedding that encodes the diffusion step for each perturbed point. The generative head then conditions on the unperturbed portion of the event to reconstruct the perturbed inputs, effectively learning an inverse diffusion denoising task. This type of masked inpainting, with a self-supervised objective, has been shown to improve representation learning in image-based and point-based models [35, 36]. In high-energy physics applications, the same mechanism can also be used for complete event generation by fully perturbing the point cloud, enabling rapid background simulation [37].

The supervised generative head follows the same Transformer-based design but is trained with a distinct objective: reconstructing invisible objects, such as neutrinos. Rather than using stochastic masking, we inject noised tokens corresponding to the undetectable components into the point cloud and train the model to denoise them conditioned on the observed objects. This diffusion-based supervised formulation has achieved state-of-the-art performance in multi-neutrino reconstruction [38], enabling the model to capture correlations between observed and unobserved event components. Formally, we align this supervised objective with our self-supervised learning. From the perspective of the backbone, recovering invisible particles (e.g., neutrinos) is structurally identical to recovering masked tokens in a self-supervised task; both are solved as diffusion-conditioned denoising. This algorithmic alignment allows the model to leverage a shared mechanism for understanding event topology, while task-specific decoders preserve their distinct targets. Both objectives use the loss in the form of Eq. 4, where  $\mathbf{v}$  and  $\mathbf{v}_{\text{pred}}$  denote the target and predicted diffusion vectors, respectively.

$$\mathcal{L}_{\text{generation}} = \|\mathbf{v} - \mathbf{v}_{\text{pred}}\|_2^2 \quad (4)$$

### C. Training procedure, software, and hardware

Model training was conducted on the *Perlmutter* supercomputer at the National Energy Research Scientific Computing Centre (NERSC), using 512 NVIDIA A100 GPUs and 16,384 CPU cores. The model implementation is based on PyTorch 2.6 [39] with PyTorch Lightning for modular training control and the Ray [40] distributed runtime for multi-node orchestration.

Pretraining employed a two-stage curriculum designed to learn latent event structures before supervised specialisation. In the first stage, the network was trained in a fully self-supervised mode with masked inputs. Only the self-supervised learning (SSL) generative head was active, and a stochastic masking probability was gradually increased during training. This procedure encouraged the encoder to reconstruct masked particle features and capture global event correlations.

In the second stage, all weights from the SSL phase were reused, and the full network was trained jointly with the classification, supervised-generative, and self-supervised-generative heads. This configuration constitutes the EVENET pretraining setup used for all downstream analyses, as summarised in Table II.

Losses from all active heads were summed directly, without gradient surgery or adaptive weighting, as empirical checks indicated that their gradient directions were not conflicting. Each loss term was internally normalised by the number of contributing processes or particles to keep magnitudes comparable across heads. Training used the LION optimiser [41] with exponential-moving-average (EMA) updates and a cosine warm-up/decay schedule. The base learning rates were  $1.8 \times 10^{-5}$  and  $1.2 \times 10^{-5}$  for the first and second stages, respectively; the effective rate scaled with  $\sqrt{N_{\text{GPU}}=512}$ , while the weight decay followed the inverse scaling,  $10^{-3}/\sqrt{512}$ .

During downstream fine-tuning, both encoder and decoder were optimised jointly, but the encoder used a learning rate one order of magnitude smaller than the

decoder to preserve pretrained representations while allowing adaptation to new tasks.

#### D. Pretrain Strategy Selection

To assess the impact of pretraining, we consider three variants of the EVENET architecture that differ only in their initialisation and training objectives:

- **EVENET-Scratch (Scratch)** is trained entirely from random initialisation and serves as a baseline representing performance without any pretraining.
- **EVENET-SSL (SSL)** is initialized from Stage 1 pretraining, which relies exclusively on self-supervised learning. This variant isolates the contribution of representation learning driven by unlabelled consistency objectives.
- **EVENET-Full (Full)** builds upon the SSL initialisation with Stage 2 pretraining, incorporating physics-supervised objectives by jointly optimising classification and supervised generation tasks together with the self-supervised loss, as detailed in Sec. II C.

These variants are evaluated consistently across all downstream studies, enabling a controlled comparison of initialisation effects without confounding architectural differences. In each downstream task, we assess performance over a broad range of training sample sizes, spanning both low- and high-statistics regimes. Training sizes are reported as multiples of a task-specific reference to account for differences in absolute event counts across analyses.

### III. SEARCH FOR A HEAVY SCALAR DECAYING TO A HIGGS BOSON AND A LIGHT SCALAR

A classic example where foundation models provide substantial benefits is the search for new physics in models with multiple free parameters that can only be constrained experimentally. Such analyses often require scanning a multi-dimensional phase space, resulting in hundreds of signal hypotheses. This places a premium on learning frameworks that remain robust across a wide range of kinematic regimes. We illustrate this task using a search for a heavy resonance decaying into a light scalar and the SM Higgs boson ( $X \rightarrow YH_{\text{SM}}$ ). Such signatures are generically predicted in a wide range of beyond SM scenarios and constitute a well-established and extensively studied benchmark for new physics searches [42–44], making them an ideal test case for assessing the generalisation and computational efficiency of foundation models. Furthermore, we evaluate this task on CMS Open Data to probe not only the foundation model’s out-of-distribution generalisation to signal processes, which

are not included in pretraining, but also to pile-up and detector-induced shifts.

A defining challenge of this class of searches is that signal statistics are limited at most mass points, as dense scans must distribute a limited full detector simulation budget across many hypotheses. By contrast, the corresponding background samples remain large and relatively unchanged across the grid. Training separate models per mass point, therefore, creates highly imbalanced learning problems, not only in terms of event weights, but more critically due to the scarcity of signal training examples that cannot be mitigated by reweighting alone. This makes per-point training both statistically inefficient and computationally expensive: convergence is slow due to the dominance of background events, and the overall resource cost can grow rapidly with the number of hypotheses. Traditional approaches attempt to address this by either training independent models for each mass point or by selecting a small subset of high-statistics points to construct a parameterized model that extrapolates across the grid, which can be challenging when the grid spans regions with markedly different signal kinematics and topologies, often at the expense of optimal sensitivity.

We focus on the  $X \rightarrow YH_{\text{SM}}$  topology with  $Y \rightarrow b\bar{b}$  and  $H_{\text{SM}} \rightarrow WW^* \rightarrow \ell\nu qq$ . Existing searches predominantly target channels such as  $b\bar{b}b\bar{b}$ ,  $b\bar{b}\gamma\gamma$ , and  $b\bar{b}\tau^+\tau^-$  [45–48], which benefit from either fully reconstructable final states or cleaner experimental signatures. The  $b\bar{b}WW$  final state, by contrast, has a comparatively large branching fraction, comparable to  $b\bar{b}b\bar{b}$ , but is significantly more challenging due to the presence of neutrinos and hadronic  $W$  decays, where the absence of heavy-flavour jets leads to large backgrounds from light-flavour quark production. These features make  $b\bar{b}WW$  a well-motivated yet experimentally demanding channel, and an ideal testbed for foundation models designed to learn robust, global event representations in complex topologies.

Simulated events are taken from the CMS Open Data release corresponding to proton–proton collisions at  $\sqrt{s} = 13$  TeV recorded in 2015–2016 [49–53]. We consider only full-simulated samples using the CMS detector [54] and restrict the study to the resolved regime with  $M_X < 1$  TeV. Signal events correspond to the process  $X \rightarrow YH_{\text{SM}} \rightarrow b\bar{b}WW^* \rightarrow b\bar{b} + \ell\nu qq$ , generated at 121 mass points spanning the  $(M_X, M_Y)$  plane. The complete list of CMS Open Data signal datasets and their corresponding DOI links is provided in Appendix A. As this study focuses on demonstrating the representational and generalisation capabilities of foundation models, only the dominant SM backgrounds are included:  $t\bar{t}$  with single-lepton decays, Drell–Yan production with heavy-flavour jets, and single-top processes in the  $s$ -,  $t$ -, and  $tW$ -channels. The simulated samples used in this analysis are summarised in Table III.

Events are reconstructed in the resolved topology and required to contain exactly one lepton and no hadroni-

Table II: Pretraining and downstream training configurations. A checkmark (✓) indicates that the corresponding network head was used in the training. **Cls**: classification; **Seg**: per-particle segmentation; **Asn**: permutation-based particle-resonance assignment; **SSL**: self-supervised generative head (masked-reconstruction); **Sup-Gen**: supervised generative head. **Base LR** is the learning rate before linear scaling with world size ( $\text{LR}_{\text{eff}} = \text{Base LR} \times \sqrt{N_{\text{GPU}}}$ ); **Model Size** reports trainable encoder and decoder parameters (in millions). **Task 1**: grid study of resonance search with two different training methods. **Task 2**: new-physics search using exotic Higgs decays; **Task 3**: quantum-correlation measurement in dileptonic top-quark pair events; **Task 4**: collision-data anomaly detection via point-cloud generation.

Category	Cls	Seg	Asn	SS-Gen	Sup-Gen	Base LR	Optimizer	GPUs	Model Size [M]
<b>Pretraining Stages</b>									
Stage I (SSL)	✗	✗	✗	✓	✗	$1.8 \times 10^{-5}$	LION	512	$18.8 + 1.3$
Stage II (Full)	✓	✗	✗	✓	✓	$1.2 \times 10^{-5}$	LION	512	$18.8 + 3.8$
<b>Downstream Tasks</b>									
Task 1 (individual)	✓	✗	✗	✗	✗	$3.0 \times 10^{-4}$	AdamW	1	$6.3 + 1.2$
Task 1 (parameterized)	✓	✗	✗	✗	✗	$1.0 \times 10^{-5}$	AdamW	2	$18.8 + 1.2$
Task 2	✓	✓	✓	✗	✗	$4.0 \times 10^{-4}$	AdamW	4	$18.8 + 8.7$
Task 3	✗	✗	✓	✗	✓	$5.0 \times 10^{-5}$	AdamW	16	$18.8 + 6.8$
Task 4	✗	✗	✗	✓	✗	$5.0 \times 10^{-4}$	AdamW	4	$18.8 + 1.7$

Table III: Simulated samples used in the  $X \rightarrow Y H_{\text{SM}} \rightarrow b\bar{b}WW^*$  analysis from 2016 CMS Open Data Simulation. For signal samples, cross sections, and total generated events vary across mass points and are not shown.

Sample	CMS Open Data dataset	$\sigma$ [pb]	$N_{\text{events}}$
tt1l	TTToSemiLeptonic_TuneCP5_13TeV-powheg-pythia8 [55]	365.35	$1.45 \times 10^8$
DYBJets_100-200	DYBJetsToLL_M-50_Zpt-100to200_TuneCP5_13TeV-madgraphMLM-pythia8 [56]	3.222	$8.85 \times 10^6$
DYBJets_200-∞	DYBJetsToLL_M-50_Zpt-200toInf_TuneCP5_13TeV-madgraphMLM-pythia8 [57]	0.618	$8.87 \times 10^5$
SingleTop_s	ST_s-channel_4f_leptonDecays_TuneCP5_13TeV-amcatnlo-pythia8 [58]	3.36	$5.47 \times 10^6$
SingleTop_t	ST_t-channel_top_4f_InclusiveDecays_TuneCP5CR1_13TeV-powheg-madspin-pythia8 [59]	136	$2.54 \times 10^7$
SingleAntiTop_t	ST_t-channel_antitop_4f_InclusiveDecays_TuneCP5_13TeV-powheg-madspin-pythia8 [60]	81	$3.06 \times 10^7$
tW_top	ST_tW_top_5f_inclusiveDecays_TuneCP5_13TeV-powheg-pythia8 [61]	35.8	$2.49 \times 10^6$
tW_antitop	ST_tW_antitop_5f_inclusiveDecays_TuneCP5_13TeV-powheg-pythia8 [62]	35.8	$2.55 \times 10^6$
Signal	NMSSM_XToYHTo2B2WTo2B2Q1L1Nu* [53]	—	—

cally decaying  $\tau$  candidates. Electrons are required to satisfy  $p_T > 35$  GeV and  $|\eta| < 2.5$ , and muons are required to satisfy  $p_T > 30$  GeV and  $|\eta| < 2.4$ . Jets are reconstructed with  $p_T > 20$  GeV and  $|\eta| < 2.4$ . Hadronically decaying  $\tau$  leptons are required to satisfy  $p_T > 30$  GeV and  $|\eta| < 2.3$ .

To avoid double counting,  $\tau$  candidates within  $\Delta R < 0.4$  of selected electrons or muons are removed. Jets within  $\Delta R < 0.4$  of selected electrons, muons, or remaining  $\tau$  candidates are removed. Selected events are required to contain at least two  $b$ -tagged jets and at least two light jets, consistent with the  $X \rightarrow Y H_{\text{SM}} \rightarrow b\bar{b}, WW^* \rightarrow b\bar{b}, \ell\nu qq$  topology, and to satisfy  $\Delta R(\ell, j_{\text{near}}) < 1.6$ , where  $j_{\text{near}}$  denotes the light jet closest to the lepton. To suppress the dominant  $t\bar{t}$  background, a topness discriminator based on a kinematic reconstruction of the semileptonic top-quark hypothesis is applied. It is defined as the minimum  $\chi^2$  over all jet assignments to the leptonic and hadronic top candidates, and events are required to satisfy topness  $> 3$ .

As baselines, we consider XGBoost [63], a boosted decision tree method widely used in HEP, and TabPFN [64,

65], a recent foundation model for tabular data. Both methods are trained on the same engineered tabular feature set.

XGBoost follows standard gradient-boosted decision tree training procedures. TabPFN is trained using version v2.5 [65]. Due to architectural constraints, the total number of training events for TabPFN is capped at 50,000. To preserve signal statistics, down-sampling is applied only to background events. We use the default ensemble of eight models together with class balancing.

Both methods operate on an identical set of engineered tabular features constructed from reconstructed objects and composite candidates. The features encode low-level kinematics of individual objects, invariant and transverse masses of physically motivated composite systems, angular correlations, and topness-related variables. For each event, two alternative hadronic- $W$  hypotheses (on-shell and off-shell  $W_{\text{had}}$ ) are considered, and all variables associated with both hypotheses are included simultaneously in the tabular input, summarised in Tab. IV.

To assess gains in sensitivity and resource efficiency, we compare EVENET against TabPFN and XGBoost using

Table IV: Tabular input variables used for the XGBoost and TabPFN baseline models. Both models are trained on an identical feature set. Here  $\ell$  denotes the selected charged lepton,  $\vec{p}_T^{\text{miss}}$  the missing transverse momentum,  $b_1, b_2$  the two highest DeepFlavour  $b$ -tagged jets, and  $q_1^h, q_2^h$  the light-jet pair forming the hadronic- $W$  candidate under hypothesis  $h$ . Two alternative hypotheses are used to assign the two light jets to the hadronic decay in the  $H_{\text{SM}} \rightarrow WW$  system. In hypothesis (A), the hadronic  $W$  candidate is formed from the pair of light jets whose invariant mass is closest to the on-shell  $W$ -boson mass, targeting the  $W_{\text{had}} \rightarrow q\bar{q}$  decay. In hypothesis (B), the light-jet pair is chosen such that the reconstructed invariant mass of the  $\ell\nu q\bar{q}$  system is closest to the Higgs boson mass. In this case, the neutrino longitudinal momentum is obtained by imposing the on-shell  $W$ -mass constraint on the leptonic  $W \rightarrow \ell\nu$  decay. Kinematic quantities are computed under both hypotheses and included as separate input features. Cluster transverse masses  $m_T$  are computed by combining the visible system with  $\vec{p}_T^{\text{miss}}$ . In addition, the topness-related variables are reconstructed under the single-lepton  $t\bar{t}$  hypothesis.

Feature group	Variables
Event-level	$\vec{p}_T^{\text{miss}}$ ; number of $b$ -tagged jets $N_b$
Lepton ( $\ell$ )	$\vec{p}_T^\ell, \eta^\ell; m_T(\ell, \vec{p}_T^{\text{miss}})$
$b$ -jet system ( $b_1, b_2$ )	$\vec{p}_T^{b_i}, \eta^{b_i}; m_{bb}; \Delta R(b_1, b_2)$
Hadronic- $W$ candidate	$\vec{p}_T^{q_i^h}, \eta^{q_i^h} (i = 1, 2); m_{W_{\text{had}}} = m(q_1^h q_2^h); p_T^{W_{\text{had}}}; \Delta R(q_1^h, q_2^h)$
Visible $WW$ system	$m_{WW}^{\text{vis}, H} = m(\ell + W_{\text{had}}); \Delta R(\ell, W_{\text{had}}); m_T(WW_{\text{had}})$
Visible $bbWW$ system	$m_{bbWW}^{\text{vis}, h} = m(bb + \ell + W_h); \Delta R(bb, \ell + W_h); m_T(bbWW_h)$
Cross-system correlations	$ \Delta\phi(bb, W_h) ; \min\{\Delta R(\ell, q_1^h), \Delta R(\ell, q_2^h)\}$
Topness	$\min \chi^2; \Delta R(\ell, b_{\text{lep}}); m(\ell, b_{\text{lep}}); m(t_{\text{lep}}); m(W_{\text{had}}); \Delta R(q_1, q_2); m(t_{\text{had}}); \Delta R(W_{\text{had}}, b_{\text{had}})$

three training variants (Sec. II D) under two configurations: (i) individual training per mass point and (ii) a single parametrized model incorporating the hypothesis masses as input features. All models are trained and evaluated on independent  $X \rightarrow Y H_{\text{SM}}$  samples with 1000 to 10,000 signal events per mass point, depending on the mass hypothesis.

For individual mass-point training, the backbone is mostly frozen: only the last layers are partially unfrozen and updated with a learning rate set to 0.3 times the base learning rate, and lightweight adapter modules inserted between transformer blocks are trained [66], reducing the number of trainable parameters from approximately 20M to 8M and stabilising training in the low-statistics regime. For parametrized training, a partial-freeze strategy is adopted, allowing backbone parameters to update with a learning rate ten times smaller than that of the task-specific heads.

Performance is evaluated using the Significance-Improvement Characteristic (SIC), defined as the signal efficiency divided by the square root of the background efficiency, with a minimum background yield of 10 events enforced to suppress statistical fluctuations [67].

As shown in Fig. 2a, EVENET-Full with individual fine-tuning achieves the highest sensitivity across essentially the entire  $(m_X, m_Y)$  mass grid. Among all training strategies considered, it consistently attains the largest maximum SIC, with only a small number of mass points exhibiting performance comparable to strong tabular baselines. Even in these cases, the differences remain within statistical uncertainties, indicating no systematic loss of sensitivity.

A key feature emerges in the low- $m_Y$  and low- $m_X$  region, where available signal statistics are extremely lim-

ited, reaching as low as  $\sim$ 1–2 k signal events per mass point. In this regime, models trained from scratch fail to learn robust decision boundaries, as reflected by the degraded sensitivity of EVENET-Scratch. This limitation is further corroborated by the training dynamics: scratch models require substantially more optimisation steps to reach their minimum validation loss, converging only after  $\sim$ 3 k steps on average. In contrast, the pretrained EVENET-Full model not only maintains strong sensitivity but also converges significantly faster, typically reaching optimal performance within  $\sim$ 1 k steps. This corresponds to an approximate factor-of-three improvement in convergence speed, highlighting the efficiency gains enabled by transferable representations.

Quantitatively, the ratio panel indicates that EVENET-Full exceeds EVENET-Scratch by roughly 50%, outperforms XGBoost by about 20% on average, and improves over TabPFN by approximately 10% across the mass grid.

Turning to parameterized training, Fig. 2b reveals that jointly trained models do not surpass the performance of individually optimised ones. Parameterized variants of both EVENET-Full and XGBoost exhibit systematically reduced sensitivity and frequently fall below the corresponding per-mass-point baselines. Notably, the individually fine-tuned EVENET-Full model remains competitive with, and often superior to, all parameterized approaches, including its own parameterized counterpart. This behaviour suggests that, for the complex  $bbWW^*$  final state, the kinematic diversity across the mass grid limits the effectiveness of parameter sharing, making local optimisation essential.

Taken together, these results establish that individually fine-tuned foundation models provide the most reli-

able and performant strategy for this class of searches. The consistent advantage of EVENET-Full in low-statistics regions highlights its strong transferability and generalisation, even when fine-tuned on realistic detector-level simulations. Despite being pretrained on fast simulation with a generic detector design, EVENET-Full adapts robustly to full CMS detector effects, underscoring the potential of foundation models to enhance sensitivity while reducing reliance on extensive dedicated simulations and repeated retraining across signal hypotheses.

#### IV. SEARCH FOR EXOTIC HIGGS BOSON DECAYS

We selected the search for exotic Higgs boson decays as another experimental testbed for assessing out-of-distribution performance. Despite more than a decade of intensive studies since the Higgs boson’s discovery in 2012, current measurements only constrain its percentage of invisible decay to below 12% [68]. Direct searches for exotic Higgs decays, therefore, remain the most sensitive probe of new physics in the Higgs sector [69]. These searches usually require two specialised models: (i) a classifier to separate new particle signal from SM backgrounds and (ii) an assignment model to reconstruct the correct decay topology by pairing reconstructed objects, an auxiliary task that strongly enhances classification performance [70].

We focus on Higgs signatures involving four bottom quarks produced through a cascade decay of  $H_{\text{SM}} \rightarrow aa \rightarrow 4b$  [71–73]. In this final state, limited light-jet rejection capability, coupled with a large QCD background, often leads to misidentified jets, thereby reducing the effectiveness of standard reconstruction and jet-resonance assignment. ML techniques provide a flexible way to resolve these ambiguities and capture correlations that fixed rules cannot. This work uses this process as a case study to evaluate pretrained foundation models on a new and challenging signature, testing their generalizability. The presence of dominant QCD backgrounds further underscores the need for precise jet assignment in isolating potential signals.

Events are required to contain at least four jets with  $p_T > 30$  GeV. At least three  $b$ -tagged jets with  $p_T > 20$  GeV are also required, with the subleading  $b$  jet satisfying  $p_T > 30$  GeV. The  $b$ -jet thresholds are defined independently of the jet requirement to remain compatible with the general high-level trigger selection. Simulated samples include  $H_{\text{SM}} \rightarrow aa$  signal events with  $m_a = 30$  GeV, along with dominant backgrounds from  $bbj$ ,  $b\bar{b}jj$ , and  $bbb\bar{b}$  processes (Tab I).

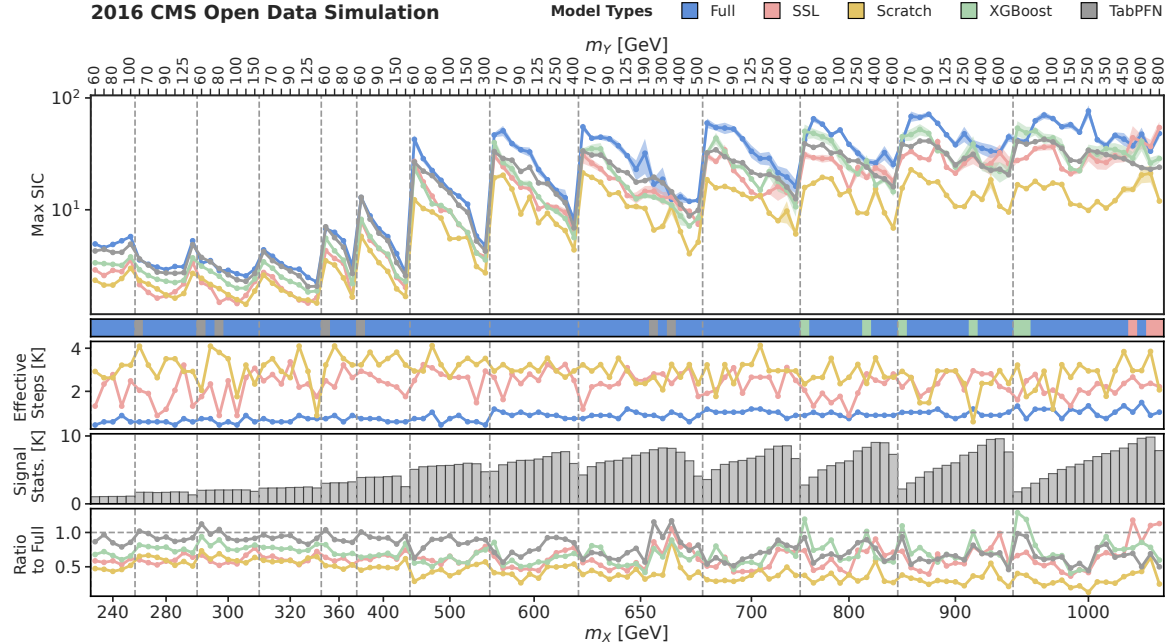
We follow the same comparison setup as in Sec. III, comparing the three EveNet training variants with the baseline SPANet [6], with matched main-body capacities of approximately 20M parameters. For EVENET-Full and EVENET-SSL, the backbone learning rate is reduced to 10% of the base value to preserve learned representa-

tions. For the transformer layers that bridge the backbone and the final heads, the learning rate is set to 30% of the base value; this intermediate scaling avoids a sudden jump in learning rate between the backbone and the heads and is found to stabilise training. All models are optimised using AdamW for 50 epochs (100 epochs for training dataset size smaller than 99k) with early stopping, using a patience of 20 epochs, and are trained on subsets of varying size drawn from the full dataset, with sample weights rescaled to reflect physical cross sections. We also tested enabling the assignment head or segmentation head alongside the classification head. In general, the inclusion of these auxiliary heads is expected to improve classification performance. Performance across different metrics is shown in Fig. 3.

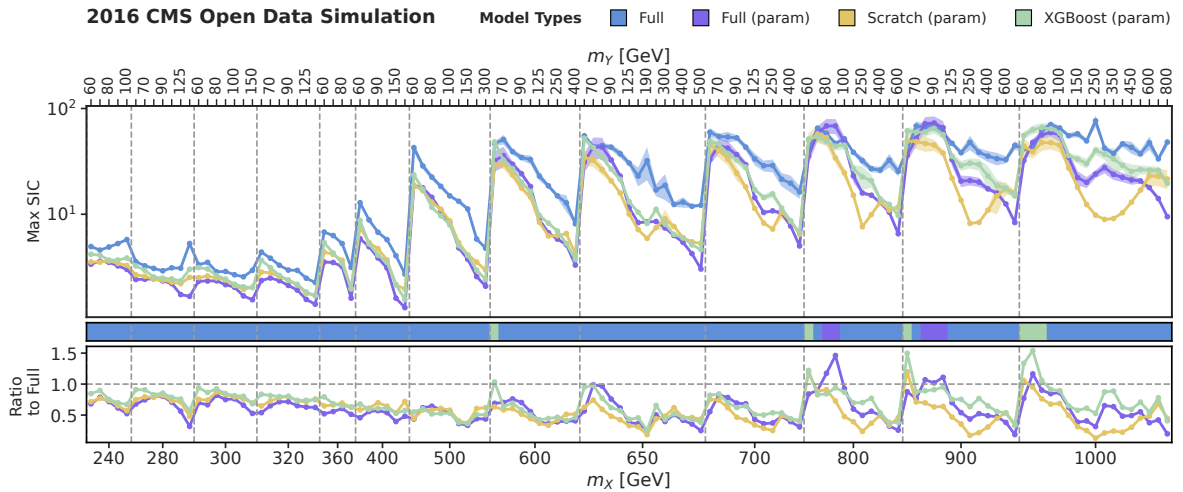
To assess the extent of task-specific supervision required, we evaluate three fine-tuning configurations: classification only (Cls), where the model is trained solely to discriminate exotic Higgs decays from SM background processes; classification with auxiliary assignment (Cls+Asn); and classification with auxiliary segmentation (Cls+Seg). In the latter two configurations, the primary classification objective is trained jointly with an auxiliary task that predicts which reconstructed objects originate from the same parent resonance.

EVENET substantially outperforms the state-of-the-art SPANet. Performance is quantified using the SIC. All models are trained and evaluated on independent samples of exotic Higgs decay (300,000 events each). Joint training of the classification and particle-pairing tasks yields visible gains (Fig. 3(a)), especially for the model trained from scratch and for SPANet. In contrast, with Full pretraining, EVENET shows only marginal differences within uncertainties across all fine-tuning configurations (Cls, Cls+Asn, and Cls+Seg). For SSL pretraining, the overall joint-optimisation gain is broadly intermediate between training from scratch and Full pretraining across the dataset-size scan. At the signal efficiency selection that maximizes SIC, the fine-tuned foundation model (Cls), EVENET-Full, achieves  $\text{SIC} = 4.1$ , far surpassing the from-scratch baseline ( $\text{SIC} = 1.6$ ) and SPANet ( $\text{SIC} = 1.4$ ).

Furthermore, EVENET-Full(Cls) shows improved performance in limited-data analysis across the full range of training dataset sizes. SPANet with an SIC of 1.3 on 5% of the total dataset shows a borderline advantage over EVENET trained from scratch ( $\text{SIC} = 1.2$ ). However, EVENET-Full consistently outperformed all other models across all dataset sizes. In particular, in the low-statistics regime (5% of the full dataset), EVENET-Full still achieves  $\text{SIC} = 1.7$ , exceeding the peak performance of both baselines trained on the full dataset. Besides SIC, the same trend can be observed in the performance of assignment tasks. EVENET-Full(Cls+Asn) rises smoothly from pairing efficiency 58% to nearly 77% as the training data increase. Compared with the pairing efficiency between EVENET-Scratch and EVENET-Full, we observe that the foundational model has already been



(a) Individual training at each mass point.



(b) Individual training (EVENET-Full) and parameterized training across the full mass grid.

Figure 2: **Sensitivity across the  $(m_X, m_Y)$  grid for  $X \rightarrow Y H_{\text{SM}}$  with  $Y \rightarrow b\bar{b}$  and  $H_{\text{SM}} \rightarrow WW^*$ .** For the individual training configuration, the figure shows five panels: (i) the maximum SIC, evaluated with a minimum background yield of 10 events, as a function of  $m_X$  (with  $m_Y$  indicated by the top axis); (ii) a per-bin “winner” map indicating the method achieving the highest maximum SIC; (iii) the effective number of optimisation steps required to reach the minimum validation loss; (iv) the available signal statistics per mass point; and (v) the ratio of the maximum SIC of each baseline method to that of the pretrained EVENET-Full. For the parameterized training configuration across the full mass grid, only panels (i), (ii), and (v) are shown, since direct loss comparisons between training strategies are not meaningful and the signal statistics are identical to those in the individual-training case.

able to extrapolate to out-of-distribution exotic Higgs decay topologies with limited data (5% of the full dataset). In contrast, SPANet starts at 26% and, under the same dataset-size constraints, never reaches the same level as EVENET-Full. Because this exotic Higgs boson decay topology is absent from the pretraining data, the strong

performance demonstrates that EVENET-Full generalises effectively to previously unseen particle decay patterns.

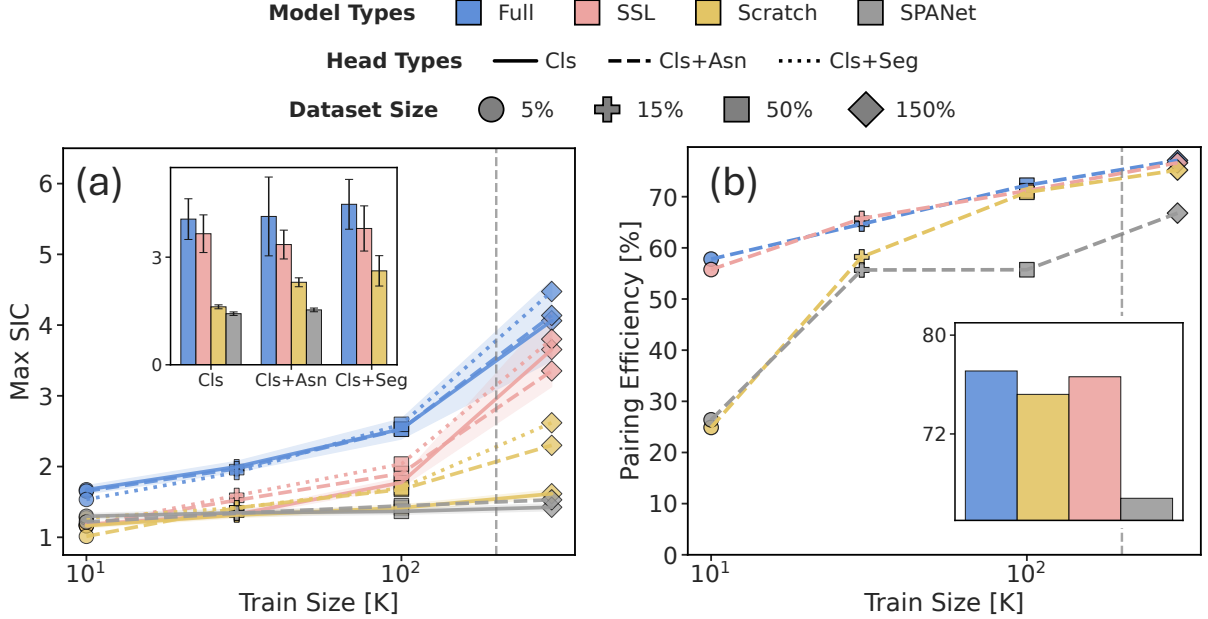


Figure 3: **Out-of-distribution generalisation to exotic Higgs-boson decays.** (a) Maximum Significance-Improvement Characteristic and (b) pairing efficiency as a function of training sample size, expressed relative to a typical search for new physics dataset of 200 K events. Blue markers denote EVENET-Full, yellow indicates training from scratch, pink corresponds to SSL pretraining, and grey shows SPANet as the comparison benchmark. Circular, cross, square, and diamond markers represent 5%, 15%, 50%, and 150% of the typical dataset size, respectively; the vertical dashed line denotes the 100% reference scale. Solid lines indicate fine-tuning only the classification head, while dashed(dotted) lines include both classification and assignment(segmentation) heads. For both panels, scatter points show performance scaling with dataset size, and the inset bar plots provide zoomed comparisons at the largest training fraction (150%).

## V. QUANTUM CORRELATIONS IN TOP-QUARK PAIRS

To evaluate EVENET in a precision regime where training data are abundant, and the relevant physics lies within the support of the pretraining distribution, we study quantum correlations in dileptonic top-quark pair production ( $t\bar{t}$ ). This task represents a high-statistics downstream setting, with typical datasets at the million-event scale, characteristic of precision SM measurements. Accurate performance in this regime depends on resolving subtle kinematic correlations rather than broad generalisation, making it a stringent benchmark for assessing how well the pretrained representation captures the detailed structure of QCD production and decay.

The top quark provides a unique laboratory for study-

ing quantum-mechanical spin correlations at the highest accessible energies. Because it decays before hadronisation, information about its spin is preserved in the angular distributions of its decay products. In dileptonic decays, the charged leptons act as near-optimal spin analysers, enabling direct access to the underlying spin structure of the production process. This feature motivated early proposals to probe quantum correlations in dileptonic  $t\bar{t}$  events, later developed into detailed phenomenological studies [74, 75] and, more recently, into experimental measurements by the ATLAS and CMS collaborations [76, 77].

In dileptonic  $t\bar{t}$  production, the spin degrees of freedom of the top–antitop pair form a two-qubit mixed quantum state described by a spin density matrix  $\rho$ . In the  $(t, \bar{t})$  spin space,  $\rho$  admits the Fano–Bloch decomposition [78]

$$\rho = \frac{1}{4} \left( \mathbb{I}_2 \otimes \mathbb{I}_2 + \sum_i B_i^+ \sigma_i \otimes \mathbb{I}_2 + \sum_j B_j^- \mathbb{I}_2 \otimes \sigma_j + \sum_{ij} C_{ij} \sigma_i \otimes \sigma_j \right), \quad (5)$$

where the coefficients  $C_{ij}$  encode the spin correlations

between the top and antitop and constitute the primary

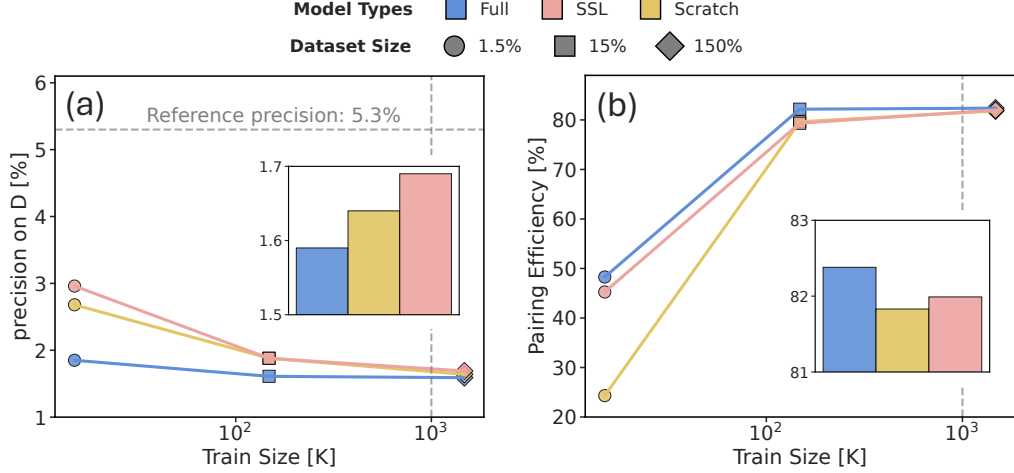


Figure 4: **Precision measurement of quantum correlations in top-quark pairs.** (a) Precision on the entanglement-sensitive observable  $D$ . (b) lepton–quark pairing accuracy as a function of training sample size, shown as a fraction of a typical dileptonic  $t\bar{t}$  analysis dataset, and Blue markers denote EVENET–Full, yellow markers indicate training from scratch, and pink markers correspond to the SSL-pretrained variant. Circular markers represent training with 1.5% of typical dataset statistics, square markers correspond to 15%, and diamond markers denote 150%; the vertical dashed line marks the 100% scale, corresponding to 1 M events commonly available in LHC precision measurements. For both panels, the main scatter plot shows performance evolution with training size, while the inset bar plots present zoomed-in comparisons for the largest training point (150%) to highlight the residual differences in model performance.

physics quantities of interest in this study; the polarisation terms  $B^\pm$  are expected to be negligible in  $t\bar{t}$  production at the LHC and are therefore ignored.

At the LHC, the spins of the top quarks are not observed directly but are accessed through the angular dis-

tributions of their decay products, whose sensitivity to the parent spin is quantified by a spin-analysing power. For an analyser  $A$  in the top decay and  $B$  in the antitop decay, such as the charged leptons in dileptonic events, with spin-analysing powers  $\kappa_A$  and  $\kappa_B$ , the normalised double-differential angular distribution is given by

$$\frac{1}{\sigma} \frac{d\sigma}{d \cos \theta_{A,i} d \cos \theta_{B,j}} = -\frac{1}{2} (1 + \kappa_A \kappa_B C_{ij} \cos \theta_{A,i} \cos \theta_{B,j}) \log |\cos \theta_{A,i} \cos \theta_{B,j}|, \quad (6)$$

where  $\theta_{A,i}$  and  $\theta_{B,j}$  denote the angles between the analyser momenta in the respective parent rest frames and the chosen spin-quantisation axes, taken here to be the helicity basis. This expression makes explicit how each element  $C_{ij}$  governs a specific angular correlation pattern, which can be extracted using angular moments, asymmetries, or likelihood fits.

While experimental measurements require collision data and a careful treatment of detector and modelling systematics, such considerations lie beyond the scope of this work. To isolate reconstruction performance and benchmark representation quality under controlled conditions, we instead follow the simulation-based evaluation strategy of Ref. [79], using it as a quantitative baseline.

From an experimental and algorithmic perspective, the

dominant challenge lies in reconstructing the full dileptonic final state: assigning each charged lepton to its parent quark and inferring the momenta of the two neutrinos that escape detection. Both steps directly impact the accuracy with which the angles  $\theta_{A,i}$  and  $\theta_{B,j}$  can be reconstructed, and therefore the precision of the extracted  $C_{ij}$ . Classical reconstruction methods typically rely on kinematic approximations or select one solution among multiple under-constrained possibilities, limiting their sensitivity to subtle angular correlations. To address these challenges jointly, we fine-tune EVENET with two physics-structured heads: an assignment head that predicts the correct lepton–quark pairing, and a supervised generative head that infers the missing neutrino momenta directly from the learned event representation.

For the training samples used in this task, leptons are required to satisfy  $p_T > 10$  GeV, and jets are required to satisfy  $p_T > 20$  GeV. We consider at most the four leading- $p_T$  leptons and  $b$  jets, and at most six additional small- $R$  jets. For the evaluation of this downstream task, events are required to contain two  $b$  jets with  $p_T > 25$  GeV and  $|\eta| < 2.5$ , and two oppositely charged leptons that satisfy the same kinematic requirements ( $p_T > 25$  GeV and  $|\eta| < 2.5$ ). The spin-correlation matrix  $C_{ij}$  is reconstructed using the decay-angle method. For each component  $C_{ij}$ , an unfolding procedure is applied in the invariant-mass ranges of (0, 400) GeV to mitigate detector effects.

To quantify the impact of pretrained representations on quantum correlation measurements, we evaluate the observable

$$D = |C_{kk} + C_{rr}| - C_{nn}, \quad (7)$$

which indicates quantum entanglement if  $D > 1$ . We perform the study using a simulated dataset scaled to the integrated luminosity recorded by ATLAS during Run-2 [80]<sup>1</sup>, and quantify the measurement precision through  $\Delta D$ , defined as the normalised uncertainty on  $D - 1$ , ensuring direct comparability with previous work [79].

Figure 4(a) shows the  $\Delta D$  as a function of training size. With only 1.5% of the dataset, typically used in dileptonic  $t\bar{t}$  analyses, EVENET-Full already achieves  $\Delta D = 1.85\%$ , competitive with the best performance of SSL and scratch models trained on an order-of-magnitude more data. Increasing the training sample to 15% improves the precision to 1.61%, and further scaling beyond typical analysis statistics yields a stable plateau of 1.59%. Across all training sizes, the pretrained model consistently outperforms SSL ( $2.96\% \rightarrow 1.69\%$ ) and scratch baselines ( $2.68\% \rightarrow 1.64\%$ ), improving the precision on  $D$  by 70% relative to the 5.3% benchmark reported in ref. [79].

Complementary to the entanglement metric, we evaluate the lepton-quark pairing accuracy to assess event topology reconstruction. As shown in Fig. 4(b), the benefit of pretraining is most striking in limited-data conditions: at 1.5% of typical training size, EVENET-Full reaches a pairing efficiency of 48%, nearly double the scratch baseline (24%) and above the SSL model (45%). At 15%, the pretrained model reaches 82% accuracy, maintaining a several-point advantage even when trained on datasets exceeding those used in real analyses (82% for EVENET-Full vs. 80% scratch and 79% SSL). Together with the  $D$  measurement, these results show that pretraining improves both the precision of neutrino inference and the resolution of combinatorial ambiguities, enabling entanglement extraction.

## VI. ANOMALY DETECTION IN COLLISION DATA

Finally, we evaluate EVENET on collision data to determine whether a model trained exclusively on simulated events can be effectively transferred to a real experimental setting. Despite the use of high-fidelity fast simulation in HEP, there is no guarantee that performance on simulation will translate to more complex collision data records with detector hardware. For this study, we use publicly available CMS Open Data [27] and compare with the previously reported anomaly detection results [23] using the CATHODE method [81] to rediscover the established resonance,  $\Upsilon$  meson. The baseline approach [23] employs a conditional normalising flow trained on sideband events (data points in regions of dimuon invariant mass adjacent to but outside the signal region) to generate background events in the signal region conditioned on the dimuon invariant mass. In this setup, the  $\Upsilon$  resonance appears as a clear excess in the opposite-sign (OS) dimuon channel, whereas same-sign (SS) dimuons, which lack significant resonant contributions, serve as a control sample to validate the accuracy of the learned background model. We train all models on 10,640 OS events from the sidebands of CMS Open Data and evaluate performance in the signal region containing 1692 events.

In our approach, the foundation model replaces the conditional normalising flow used in the baseline with EVENET to directly generate high-dimensional dimuon point clouds. Because generative models do not automatically guarantee exact two-body kinematics, we introduce a post-generation calibration procedure that restores physical constraints such as invariant-mass closure and momentum balance. This step is essential for evaluating whether a model genuinely learns dimuon structure rather than merely producing visually plausible clouds. Models that understand the underlying physics require only minimal adjustments, whereas models lacking such knowledge collapse in performance after calibration.

This study uses the CMS Open Data DoubleMu collected in 2016 at  $\sqrt{s} = 13$  TeV to probe the anti-isolated  $\Upsilon$  family of spin-1 bottomonium ( $b\bar{b}$ ) resonances with masses  $m_\Upsilon \geq 2m_b \simeq 10$  GeV. Events are further categorised by muon charge into opposite-sign (OS) and same-sign (SS) samples, with the SS sample used for validation. To isolate the  $\Upsilon$  mesons, we define three dimuon invariant mass regions: a left sideband (5–9 GeV), a signal region (9–10.6 GeV), and a right sideband (10.6–16 GeV). The sidebands are chosen to exclude known dimuon resonances, providing clean samples for background modelling. The background probability density,  $p_{Bkg}(m)$ , is obtained by fitting a quintic polynomial to the dimuon mass distribution in the sidebands using a relative bin width of 1.5%, slightly larger than the  $\sim 1\%$  mass resolution verified from  $J/\psi$  fits [23] and consistent with previous dimuon analyses [82, 83].

To interpolate the background into the signal region, we employ an ensemble of five independently trained

<sup>1</sup> Integrated luminosity of 140  $\text{fb}^{-1}$ .

diffusion-based EVENET generative models. All three EveNet variants (Sec. II D) are evaluated. For the pre-trained models (EVENET-Full and EVENET-SSL), the backbone learning rate is reduced to 10% of the base value during fine-tuning, while the Scratch model is trained with a uniform learning rate. The sideband data are partitioned into five folds, and each model is trained on a distinct fold to ensure comprehensive coverage and statistical stability across the ensemble. The final generated background sample is obtained by taking the union of events produced by all five models. The interpolated background is constructed from the relative fold weights and combined to produce a smooth prediction in the signal region.

$$p_{\text{Bkg}}(x, m) = p_{\text{Bkg}}(x|m) p_{\text{Bkg}}(m),$$

where  $p_{\text{Bkg}}(x|m)$  is learned by the EveNet ensemble.

Event generation proceeds in two sequential stages. In the first stage, intermediate features of each event are produced by generating global observables, such as  $H_T$  and  $\Delta R(\mu_1, \mu_2)$ , conditionally on the dimuon mass. This stage captures coarse event-level correlations and serves as a bridge between the mass distribution and detailed event structure. In the second stage, the full event point cloud, representing the dimuon system and comprising kinematic and vertex-level features, is generated conditionally on the dimuon mass together with the intermediate variables  $H_T$  and  $\Delta R(\mu_1, \mu_2)$ . Global observables are then recomputed directly from the generated point clouds, and the analysis selections are reapplied. This post-processing step further enhances the physical fidelity and internal consistency of the simulated background samples.

In general, the invariant mass reconstructed from the final generated point cloud,  $m_{\text{gen}}$ , does not necessarily coincide with the conditioned dimuon mass,  $m_{\text{condition}}$ . To mitigate this discrepancy, we introduce a *calibration* method that explicitly enforces the correct dimuon kinematics by performing a reconstruction step in the dimuon rest frame (PRF). Each generated muon is treated as on-shell, with energy defined as  $E_i = \sqrt{|\vec{p}_i|^2 + m_\mu^2}$ . The event is boosted to the PRF, where the two muons are expected to be back-to-back in collision data; a calibration step is then applied to restore this configuration. The momentum magnitude is fixed according to the conditioned mass  $M$ ,

$$p^* = \sqrt{\left(\frac{M}{2}\right)^2 - m_\mu^2}, \quad E^* = \frac{M}{2},$$

and the back-to-back axis is defined as  $\hat{n} \propto \vec{p}_1^{\text{PRF}} - \vec{p}_2^{\text{PRF}}$ . The calibrated four-vectors in the PRF are then

$$p_1^{*'} = (E^*, +p^* \hat{n}), \quad p_2^{*'} = (E^*, -p^* \hat{n}),$$

which are finally boosted back to the laboratory frame. This procedure guarantees that the generated dimuon

mass equals the conditioned mass  $M$ . Physically, we rely only on the dimuon boost and decay directions in the PRF, as predicted by the generative model.

Focusing on the SR, we train an ensemble of Boosted Decision Trees (BDTs) to distinguish observed data,  $p_{\text{Data}}(x)$ , from the interpolated background,  $p_{\text{Bkg}}(x)$ . Each BDT learns an optimal sequence of feature-based splits to maximise separation between the two samples. Input features are chosen to avoid any explicit dependence on the dimuon mass, thereby preventing mass sculpting.

We assume the data distribution can be expressed as

$$p_{\text{Data}}(x) = \mu p_{\text{sig}}(x) + (1 - \mu) p_{\text{Bkg}}(x),$$

where  $\mu = \frac{N_{\text{sig}}}{N_{\text{sig}} + N_{\text{bkg}}}$  represents the signal fraction. In the asymptotic limit, the classifier score

$$z(x) = \frac{p_{\text{Data}}(x)}{p_{\text{Data}}(x) + p_{\text{Bkg}}(x)}$$

is monotonically related to the likelihood ratio

$$l(x) = \frac{z(x) - (1 - \mu)(1 - z(x))}{\mu(1 - z(x))} = \frac{p_{\text{sig}}(x)}{p_{\text{Bkg}}(x)},$$

which serves as the most powerful mass-independent test statistic. To maximise statistical power while avoiding bias, we employ five-fold cross-validation, ensuring that each classifier is evaluated on data not seen during training.

The *likelihood-reweighting* approach is used; each event  $i$  is assigned a weight  $w_i = l(x_i)$  corresponding to the estimated signal-to-background likelihood ratio. This generalises the cut-based method by continuously weighting events according to their signal-like probability. Since the estimate of  $l(x)$  may yield negative values for background-like events, we impose a mild classifier cut to exclude them (equivalently, setting negative weights to zero). The weighted mass spectrum in the sidebands is fitted to estimate the background contribution in the SR, using scaled Poisson likelihoods to account for the event weights. This weighted analysis retains higher sensitivity by exploiting the full discriminant distribution rather than a single threshold.

We evaluate the analysis under four configurations by training and testing classifiers independently on the opposite-sign (OS) and same-sign (SS) channels, yielding OS→OS, OS→SS, SS→OS, and SS→SS settings, where  $A \rightarrow B$  denotes training on  $A$  and evaluating on  $B$ . To account for statistical fluctuations and model variability throughout the analysis pipeline, we perform eight independent bootstrap experiments, each using a distinct ensemble of generative models. Within each bootstrap, 20,000 generated events are selected to train a five-fold classifier for each pseudo-experiment. A total of 200 pseudo-experiments are conducted in each bootstrap, yielding 1600 pseudo-experiments per channel.

Performance is evaluated using the  $\ell$ -reweighted median significance [23], as shown in Fig. 5(a). In the

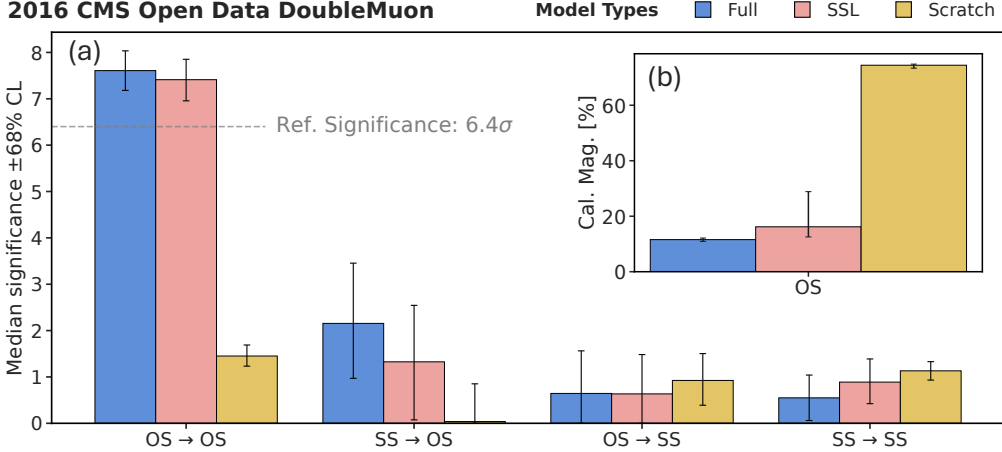


Figure 5: Collision-data anomaly detection using dimuon point-cloud generation. (a) Median  $\ell$ -reweighted anomaly significance for four train→test configurations: OS→OS, SS→OS, OS→SS, and SS→SS. Blue markers denote EVENET-Full, yellow denote models trained from scratch, pink correspond to EVENET-SSL. The horizontal dashed line marks the published reference significance. (b) Calibration magnitude required to restore exact dimuon topology, shown as the relative per-event momentum adjustment (%) in the OS region. Uncertainty bands in both panels represent the spread across eight independently trained models and statistical variation from 200 resamplings per model.

primary OS → OS configuration, where both training and evaluation include genuine  $\Upsilon \rightarrow \mu^+ \mu^-$  decays, the calibrated EVENET-Full achieves a median significance of  $7.6^{+0.4}_{-0.4}\sigma$ , surpassing the published benchmark of  $6.4\sigma$  in Ref. [23]. Importantly, its performance remains stable under the calibrated reconstruction, indicating that correct two-body kinematics are already internalised during generation. EVENET-SSL, pretrained with the same task-specific head, exhibits similar behaviour with  $7.4^{+0.4}_{-0.5}\sigma$ , though the slightly lower value suggests that full pretraining provides additional physics understanding beyond SSL alone. In contrast, the model trained from scratch performs poorly once physically consistent kinematics are enforced, achieving only  $1.45^{+0.24}_{-0.22}\sigma$ .

Control tests further validate the stability of pretrained models. Swapping the training and evaluation targets yields results consistent with zero in SS→SS and OS→SS cases, while SS→OS produces small non-zero values due to resonances present only in evaluation data. Throughout all configurations, EVENET-Full and EVENET-SSL remain stable with no evidence of mass sculpting.

Figure 5(b) visualises the magnitude of corrections required during calibration. Pretrained models require only 11%–16% adjustments to restore exact topology, indicating that they naturally encode dimuon kinematics. In contrast, the scratch model requires large 75% corrections on average, revealing that calibration not only ensures physical validity but also serves as a diagnostic for genuine physics understanding.

## VII. STABILITY STUDY ON SYSTEMATICS

Collision data are subject to reconstruction uncertainties that perturb reconstructed object kinematics, such as jet energies and missing transverse momentum. Robust foundation models must therefore maintain stable downstream performance under variations in detector response, without requiring retraining. In all studies presented here, models are trained once on the reference samples used in prior downstream-task studies and are then evaluated directly on systematically varied datasets without retraining.

We first assess systematic robustness using the exotic Higgs decay benchmark introduced in Sec. IV, where both classification sensitivity (SIC) and resonance reconstruction via jet pairing depend critically on accurate jet kinematics. To emulate detector uncertainty, we follow the systematic variation strategy of Ref. [84] and generate one hundred pseudo-experiments with jet-energy-scale (JES) shifts drawn from a Gaussian prior with a width of 1%. For each shifted sample, we re-evaluate the maximum SIC and the jet-pairing efficiency.

To isolate genuine systematic effects from statistical fluctuations, the response is quantified relative to each model’s intrinsic spread, expressed as the deviation from its mean in units of its statistical uncertainty. As shown in Fig. 6, the fully pretrained EVENET-Full exhibits substantially greater stability than the corresponding model trained from scratch. For the SIC metric, EVENET-Full varies within 0.21 (68% interval width) and 0.34 (95% interval width), compared with 0.71 and 1.42 for the scratch model. A similar trend is observed for jet-pairing efficiency, where the 95% interval remains con-

tained within 0.48 for EVENET-Full, versus 0.62 for the scratch model. These results demonstrate that pretraining significantly enhances robustness to JES variations in a search for new physics settings.

We further evaluate systematic stability in the quantum-correlation benchmark introduced in Sec. V, where entanglement is quantified through the precision of the quantum-correlation parameter  $D$ . Unlike the exotic Higgs-decay benchmark, this study probes sensitivity to both jet-related and global event-level uncertainties. Two independent sources of systematic variation are considered: JES shifts and soft missing transverse energy (MET) fluctuations, which are expected to be among the dominant experimental systematics for this task.

For the QC benchmark, we generate fifty pseudo-experiments with JES variations drawn from the same 1% Gaussian prior, and fifty additional pseudo-experiments with soft MET fluctuations implemented by adding stochastic noise to the MET magnitude, sampled from a log-normal distribution. In all cases, the model trained on the nominal sample is evaluated directly on the systematically varied data, without retraining. The response is quantified as the absolute shift in the precision of  $D$  relative to its nominal mean.

As shown in Fig. 7, EVENET-Full remains highly stable under both JES and MET variations. The spread of the precision shift is confined within  $5 \times 10^{-4}$  at 68% confidence level and  $1 \times 10^{-3}$  at 90% confidence level for both sources of uncertainty. In contrast, the model trained from scratch exhibits fluctuations that are approximately five times larger. These results demonstrate that pretraining not only improves absolute performance but also confers strong resilience to detector-level systematics, indicating that the underlying neutrino-momentum reconstruction, which dominantly controls the precision of  $D$ , remains stable under systematic variations.

Overall, across both the exotic Higgs-decay and quantum-correlation benchmarks, EVENET-Full consistently exhibits enhanced stability against detector uncertainties, underscoring its suitability for precision measurements and searches in collider data.

## VIII. TRAINING CONVERGENCE

A hallmark of effective foundation models is to reach strong optima rapidly with minimal fine-tuning. We quantify the convergence behaviour of EVENET using the minimum validation loss achieved during training and the number of effective training steps (optimiser updates scaled by GPU count and batch size) required to reach that minimum. On the quantum-correlation task, EVENET-Full consistently attains the lowest loss with substantially fewer updates than both the SSL-only and Scratch baselines. At small training sizes, EVENET-Full reaches a loss of 1.11 within  $\mathcal{O}(200)$  effective steps, whereas SSL requires a similar number of steps but

plateaus at a higher loss (1.46), and Scratch remains significantly worse (1.87). As the dataset grows, the gap in final loss narrows, yet the convergence advantage remains clear: EVENET-Full reaches its optimal plateau of 0.86 using nearly an order of magnitude fewer updates than Scratch, highlighting both faster optimisation and a lower loss floor.

An analogous trend appears in the exotic-Higgs benchmark across the Cls-only and Cls+Asn objectives. EVENET-Full consistently achieves its best validation loss at dramatically lower compute cost, reaching values of 0.40–0.45 within  $\mathcal{O}(10^2)$ – $\mathcal{O}(10^3)$  steps, whereas SSL converges more slowly and scratch requires  $\mathcal{O}(10^3)$ – $\mathcal{O}(10^4)$  steps to approach comparable performance.

Taken together, these results demonstrate that the EVENET foundation model not only yields superior final accuracy, but also significantly accelerates and stabilises fine-tuning, delivering lower loss minima with substantially reduced computational cost compared with both scratch training and SSL-only pretraining.

## IX. DISCUSSION

In this study, we present EVENET, a new foundation model designed specifically for event-level applications in HEP. We conduct benchmarking across four downstream HEP analysis settings, spanning precision measurements, searches for new physics, and including an application to collision data for anomaly detection. We demonstrate that EVENET outperforms specialised baselines across most studied regimes, often with minimal fine-tuning. Importantly, in contrast to prior approaches that have primarily centred on single discriminative objectives [18, 19], EVENET learns continuous, physics-consistent representations that remain robust under the detector and kinematic variations considered in this work.

A central insight from our work is that collider data with explicit structures benefit substantially from a **hybrid pretraining strategy**. While SSL dominates in language and vision domains, the unambiguous truth labels from physics simulations provide powerful inductive signals that guide the representation more effectively than SSL alone in our setting. This synergy between structured supervision and self-supervised consistency allows EVENET to collapse traditional multi-stage pipelines into a single, efficient backbone that supports both discriminative tasks and generative modelling.

The search for heavy Higgs across the mass grid highlights the computational efficiency of EVENET without sacrificing physics performance: a single pretrained backbone can be adapted across many scan points with minimal fine-tuning, providing a scalable alternative to training separate models per hypothesis, and even outperforms tabular foundation models across strongly varying kinematic regimes.

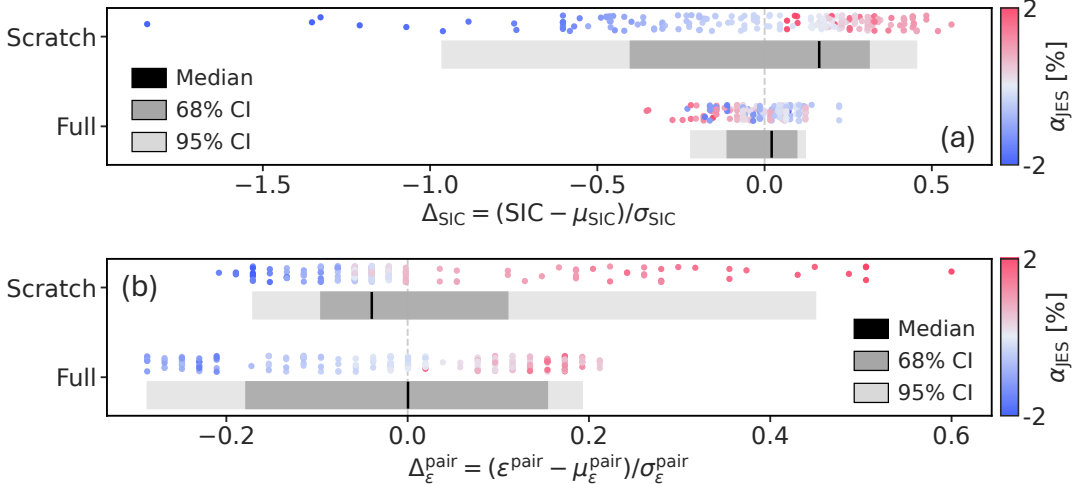


**Figure 6: Impact of JES variations on classification and jet-pairing performance for the exotic Higgs-decay benchmark.** (a) Normalised shift in maximum SIC score,  $\Delta_{\text{SIC}} = (\text{SIC} - \mu_{\text{SIC}})/\sigma_{\text{SIC}}$ , and (b) normalised shift in jet-pairing efficiency,  $\Delta_{\varepsilon}^{\text{pair}} = (\varepsilon^{\text{pair}} - \mu_{\varepsilon}^{\text{pair}})/\sigma_{\varepsilon}^{\text{pair}}$ , evaluated under systematic jet-energy-scale shifts drawn from a Gaussian prior with a width of 1%. Each point represents an individual JES variation, coloured by the JES shift parameter  $\alpha_{\text{JES}}$  from negative (blue) to positive (red). The black vertical line indicates the median response, while the dark and light grey bands correspond to the central 68% and 95% confidence intervals, respectively. Results are shown for models trained from scratch (top) and using full pretraining (bottom).

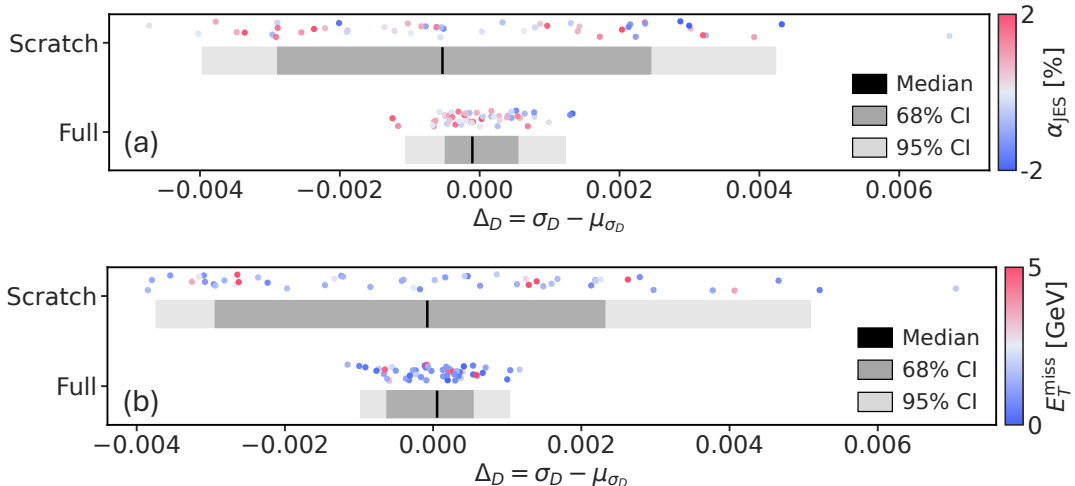


**Figure 7: Impact of JES variations and soft MET fluctuations on the precision of the quantum-correlation observable  $D$  in the quantum-correlation benchmark.** (a) Shift in the measured precision of  $D$  under systematic JES variations, where the JES nuisance parameter is sampled from a Gaussian prior with a width of 1%. (b) Shift in the measured precision of  $D$  under soft MET fluctuations, implemented by adding stochastic noise to the MET magnitude drawn from a log-normal distribution with parameters  $\mu = 0$  and  $\sigma = 1$ , and truncated to the range  $0 \leq \Delta E_T^{\text{miss}} \leq 5$  [GeV]. In both panels, the vertical axis represents the deviation of the precision from its nominal mean value. Each point corresponds to an individual systematic variation and is coloured according to the corresponding nuisance parameter value. The black vertical line denotes the median response, while the dark and light grey bands indicate the central 68% and 95% confidence intervals, respectively. Results are shown for models trained from scratch (top) and with full pretraining (bottom).

A complementary pattern emerges in the search for exotic Higgs decays. For models trained from scratch and for the SPANet baseline, incorporating an assign-

ment or segmentation head consistently improves classification performance, as expected from the known discriminative power of resonance topology. However, with

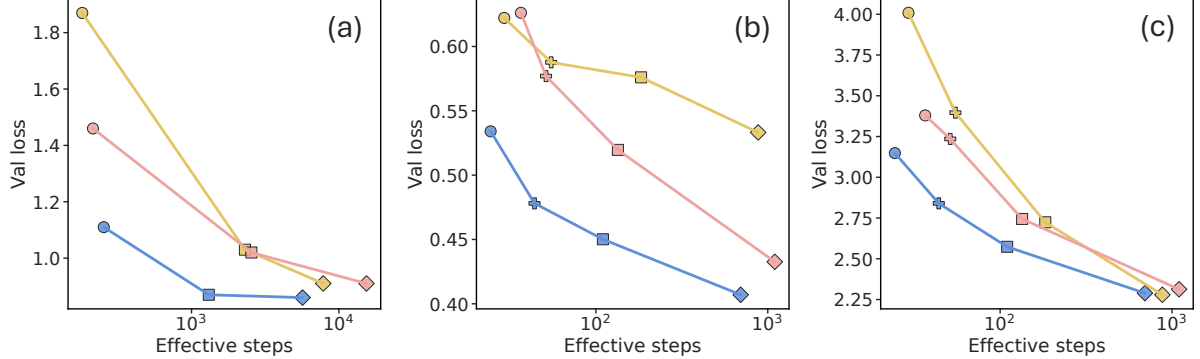


Figure 8: **Training dynamics and convergence speed.** Validation loss as a function of effective training steps for three downstream tasks. Panel (a) shows the quantum-correlation task, while Panels (b,c) correspond to the exotic Higgs benchmark using classification-only and classification+assignment objectives. Each panel shows three curves: EVENET-Full (blue), the model trained from scratch (yellow), and SSL-pretrained EVENET-SSL (pink). The x-axis represents the effective number of parameter-update steps required to reach the minimum validation loss, allowing a direct comparison of convergence speed across dataset sizes. Points along each curve correspond to models trained with different dataset sizes.

EVENET-Full, this auxiliary benefit vanishes: the classification head alone achieves one of the highest sensitivities. This demonstrates that the pretrained representation already encodes, at least implicitly, the cascade decay structure characteristic of collider events, thereby reducing the need for task-specific architectural modifications during fine-tuning, even though these auxiliary heads are not used during pretraining.

In the quantum-correlation study, the downstream objective requires the simultaneous generation of neutrino four-momenta and the assignment of resonances. Models trained from scratch overfit rapidly on these tightly coupled objectives, while two-stage pipelines introduce unnecessary complexity and require substantially greater computational resources. In contrast, EVENET-Full enables stable end-to-end training across all dataset sizes, indicating that pretraining imposes a strong inductive bias that simplifies multi-step inference. Crucially for precision measurements, this behaviour is accompanied by increased stability under the nuisance variations evaluated in this work, supporting the use of the learned representation in settings where robustness to systematics is essential.

This cross-task coherence extends beyond supervised training objectives to self-supervised generative settings on collision data. In anomaly detection, EVENET-Full maintains stable performance across detector and kinematic regimes even with limited statistics, surpassing the published benchmark (median significance:  $7.6^{+0.4}_{-0.4}\sigma$ , compared with  $6.4\sigma$  in Ref. [23]) while remaining stable under the calibrated reconstruction, consistent with physically correct two-body kinematics. In contrast, the scratch model fails once physical consistency is enforced. This suggests that the scratch model was merely memorising noise and data rather than learning the underlying

physics of the particles.

Taken together, these results underscore the value of a unified event-level representation for particle collision data analyses. By integrating structured physical supervision with self-supervised regularisation, EVENET learns representations that remain performant across diverse tasks, detector conditions, and statistical regimes. This enables the consolidation of traditionally multi-stage analyses into a single backbone, achieving high sensitivity while substantially reducing computational and methodological overhead.

Despite these advances, several critical challenges remain. While EVENET incorporates noise-tolerance training, it does not yet constitute a fully uncertainty-aware framework. The explicit modelling and propagation of detector systematics and theoretical uncertainties remain essential for achieving the rigorous statistical interpretations required for the future measurements. Similarly, while multi-head architectures prove effective, the individual outputs are not currently constrained to satisfy physical conservation laws or other exact physical symmetries, leaving room for future structured-consistency objectives. Transfer performance to collision data is encouraging, but a systematic evaluation under severe simulation mis-modelling relative to collision data has not yet been conducted. Finally, while the representation encodes event structures and kinematics, a detailed analysis of the latent space and its interpretability is left to future work.

In conclusion, EVENET demonstrates a potential event-level foundation model as a flexible and effective framework for a broad range of analyses in HEP. Deploying the model in LHC analyses using collision data will serve as the definitive test of its ability to streamline and accelerate end-to-end inference for scientific discov-

ery, particularly when integrated with object-level frameworks such as OmniLearned. Integrating EVENET with future differentiable detector simulations or fast simulation frameworks could realise fully differentiable analysis pipelines that the community has long sought for, enabling gradient-based optimisation from experimental observables directly to fundamental theory parameters. Moreover, the emergent physics-aware structure of the latent space creates new opportunities for interpretable representations and anomaly-sensitive embeddings. In the long term, models of this class may serve as building blocks for autonomous analysis systems that optimise data-taking or actively assist the search for new phenomena. Collectively, these advances position EVENET as a concrete instantiation of the event-level foundation-model approach, highlighting its potential to drive a paradigm shift in data-intensive scientific discovery.

## ACKNOWLEDGEMENTS

We gratefully acknowledge Rikab Gambhir and Radha Mastandrea for their helpful discussions and constructive feedback on the anomaly-detection analysis. VM is supported by JST EXPERT-J, Japan Grant Number JPMJEX2509. T.-H. Hsu and W.-S. Hou are supported by the National Science and Technology Council (NSTC) grant

No. 113-2639-M-002-006-ASP. Y. Xu, Y.-T. Chou, S.-C. Hsu and Y. Zhang are supported by the National Science Foundation (NSF) grant No. PHY-2117997. Q. LIU and BN are supported by the U.S. Department of Energy under contract number DE-AC02-76SF00515. This research used resources of the National Energy Research Scientific Computing Centre, a U.S. Department of Energy Office of Science User Facility supported by the Office of Science of the U.S. Department of Energy under Contract No. DE-AC02-05CH11231 using NERSC award NERSC DDR-ERCAP0034643.

## DATA AVAILABILITY

The datasets used for pretraining and finetuning, together with the pretrained EveNet model weights, are publicly accessible on at <https://huggingface.co/datasets/Avencast/EveNet>.

## CODE AVAILABILITY

The source code for EveNet and the scripts for training baseline models are openly available at <https://github.com/EveNet-HEP>. Pretraining configurations can be provided upon reasonable request.

---

[1] P. Shanahan, K. Terao, and D. Whiteson, Snowmass 2021 computational frontier compf03 topical group report: Machine learning (2022), arXiv:2209.07559.

[2] H. Qu and L. Gouskos, ParticleNet: Jet Tagging via Particle Clouds, *Phys. Rev. D* **101**, 056019 (2020).

[3] G. Kasieczka, T. Plehn, A. Butter, K. Cranmer, D. Debennath, B. M. Dillon, M. Fairbairn, D. A. Faroughy, W. Fedorko, C. Gay, L. Gouskos, J. F. Kamenik, P. T. Komiske, S. Leiss, A. Lister, S. Macaluso, E. M. Metodiev, L. Moore, B. Nachman, K. Nordström, J. Pearkes, H. Qu, Y. Rath, M. Rieger, D. Shih, J. M. Thompson, and S. Varma, The Machine Learning landscape of top taggers, *SciPost Phys.* **7**, 014 (2019).

[4] A. Bogatskiy, T. Hoffman, D. W. Miller, J. T. Offermann, and X. Liu, Explainable equivariant neural networks for particle physics: Pelican, *J. High Energy Physics* **2024**, 1 (2024).

[5] J. Pata, E. Wulff, F. Mokhtar, D. Southwick, M. Zhang, M. Girone, and J. Duarte, Improved particle-flow event reconstruction with scalable neural networks for current and future particle detectors, *Commun. Phys.* **7**, 124 (2024).

[6] M. J. Fenton, A. Shmakov, H. Okawa, Y. Li, K.-Y. Hsiao, S.-C. Hsu, D. Whiteson, and P. Baldi, Reconstruction of unstable heavy particles using deep symmetry-preserving attention networks, *Commun. Phys.* **7**, 139 (2024).

[7] G. Karagiorgi, G. Kasieczka, S. Kravitz, B. Nachman, and D. Shih, Machine learning in the search for new fundamental physics, *Nature Rev. Phys.* **4**, 399 (2022).

[8] A. Crivellin and B. Mellado, Anomalies in particle physics and their implications for physics beyond the standard model, *Nature Rev. Phys.* **6**, 294 (2024).

[9] B. M. Dillon, G. Kasieczka, H. Olschläger, T. Plehn, P. Sorrenson, and L. Vogel, Symmetries, safety, and self-supervision, *SciPost Phys.* **12**, 188 (2022).

[10] B. M. Dillon, L. Favaro, F. Feiden, T. Modak, and T. Plehn, Anomalies, representations, and self-supervision, *SciPost Phys. Core* **7**, 056 (2024).

[11] P. Harris, J. Krupa, M. Kagan, B. Maier, and N. Woodward, Resimulation-based self-supervised learning for pretraining physics foundation models, *Phys. Rev. D* **111**, 032010 (2025).

[12] T. Golling, L. Heinrich, M. Kagan, S. Klein, M. Leigh, M. Osadchy, and J. A. Raine, Masked particle modeling on sets: towards self-supervised high energy physics foundation models, *Mach. Learn. Sci. Tech.* **5**, 035074 (2024).

[13] V. Mikuni and B. Nachman, Method to simultaneously facilitate all jet physics tasks, *Phys. Rev. D* **111**, 054015 (2025).

[14] W. Bhimji, C. Harris, V. Mikuni, and B. Nachman, Omnilearned: A foundation model framework for all tasks involving jet physics (2025), arXiv:2510.24066.

[15] O. Amram, L. Anzalone, J. Birk, D. A. Faroughy, A. Hallin, G. Kasieczka, M. Krämer, I. Pang, H. Reyes-Gonzalez, and D. Shih, Aspen Open Jets: unlocking LHC data for foundation models in particle physics, *Mach. Learn. Sci. Tech.* **6**, 030601 (2025).

[16] J. Birk, A. Hallin, and G. Kasieczka, OmniJet- $\alpha$ : the first cross-task foundation model for particle physics, *Mach. Learn. Sci. Tech.* **5**, 035031 (2024).

[17] L. Tani, J. Pata, and J. Birk, Reconstructing hadronically decaying tau leptons with a jet foundation model, *SciPost Phys. Core* **8**, 046 (2025).

[18] J. Ho, B. R. Roberts, S. Han, and H. Wang, Pretrained Event Classification Model for High Energy Physics Analysis (2024), arXiv:2412.10665.

[19] A. J. Wildridge, J. P. Rodgers, E. M. Colbert, Y. yao, A. W. Jung, and M. Liu, Bumblebee: Foundation Model for Particle Physics Discovery (2024), arXiv:2412.07867.

[20] D. Park et al., FM4NPP: A Scaling Foundation Model for Nuclear and Particle Physics (2025), arXiv:2508.14087.

[21] M. Awais, M. Naseer, S. Khan, R. M. Anwer, H. Cholakkal, M. Shah, M.-H. Yang, and F. S. Khan, Foundation models defining a new era in vision: a survey and outlook, *IEEE Transactions on Pattern Analysis and Machine Intelligence* <https://doi.org/10.48550/arXiv.2307.13721> (2025).

[22] C. Zhou, Q. Li, C. Li, J. Yu, Y. Liu, G. Wang, K. Zhang, C. Ji, Q. Yan, L. He, et al., A comprehensive survey on pretrained foundation models: A history from bert to chatgpt, *International Journal of Machine Learning and Cybernetics* **16**, 9851 (2025).

[23] R. Gambhir, R. Mastandrea, B. Nachman, and J. Thaler, Isolating Unisolated Upsilon with Anomaly Detection in CMS Open Data (2025), arXiv:2502.14036.

[24] J. Alwall, R. Frederix, S. Frixione, V. Hirschi, F. Maltoni, O. Mattelaer, H.-S. Shao, T. Stelzer, P. Torrielli, and M. Zaro, The automated computation of tree-level and next-to-leading order differential cross sections, and their matching to parton shower simulations, *J. High Energy Phys.* **2014** (7), 79.

[25] T. Sjöstrand, S. Ask, J. R. Christiansen, R. Corke, N. De-sai, P. Ilten, S. Mrenna, S. Prestel, C. O. Rasmussen, and P. Z. Skands, An introduction to PYTHIA 8.2, *Computer Physics Communications* **191**, 159 (2015).

[26] The DELPHES 3 collaboration, J. De Favereau, C. Delaere, P. Demin, A. Giammanco, V. Lemaître, A. Mertens, and M. Selvaggi, DELPHES 3: a modular framework for fast simulation of a generic collider experiment, *J. High Energy Phys.* **2014** (2), 57.

[27] CMS Collaboration, DoubleMuon primary dataset in NANO AOD format from RunH of 2016, CERN Open Data Portal (2024), dataset: /DoubleMuon/Run2016H-UL2016\_MiniAODv2\_NanoAODv9-v1/NANO AOD.

[28] A. Vaswani, N. Shazeer, N. Parmar, J. Uszkoreit, L. Jones, A. N. Gomez, L. Kaiser, and I. Polosukhin, Attention Is All You Need (2023), arXiv:1706.03762.

[29] J. Ho, A. Jain, and P. Abbeel, Denoising diffusion probabilistic models (2020), arXiv:2006.11239.

[30] N. Carion, F. Massa, G. Synnaeve, N. Usunier, A. Kirillov, and S. Zagoruyko, End-to-end object detection with transformers (2020), arXiv:2005.12872.

[31] B. Cheng, I. Misra, A. G. Schwing, A. Kirillov, and R. Girdhar, Masked-attention mask transformer for universal image segmentation (2022), arXiv:2112.01527.

[32] H. Kuhn, The hungarian method for the assignment problem, *Naval Research Logistics Quarterly* **2** (2012).

[33] T.-Y. Lin, P. Goyal, R. Girshick, K. He, and P. Dollár, Focal loss for dense object detection (2018), arXiv:1708.02002.

[34] C. H. Sudre, W. Li, T. Vercauteren, S. Ourselin, and M. Jorge Cardoso, Generalised dice overlap as a deep learning loss function for highly unbalanced segmentations (2017).

[35] K. He, X. Chen, S. Xie, Y. Li, P. Dollár, and R. Girshick, Masked autoencoders are scalable vision learners (2021), arXiv:2111.06377.

[36] X. Yu, L. Tang, Y. Rao, T. Huang, J. Zhou, and J. Lu, Point-bert: Pre-training 3d point cloud transformers with masked point modeling (2022), arXiv:2111.14819.

[37] V. Mikuni, B. Nachman, and M. Pettee, Fast point cloud generation with diffusion models in high energy physics, *Phys. Rev. D* **108**, 036025 (2023).

[38] Y. Zhang, B.-H. Zhou, Q.-B. Liu, T. A. Wu, S. Li, T. Han, S.-C. Hsu, and M. Low, Entanglement and bell nonlocality in  $\tau^+\tau^-$  at the lhc using machine learning for neutrino reconstruction (2025), arXiv:2504.01496.

[39] A. Paszke, S. Gross, F. Massa, A. Lerer, J. Bradbury, G. Chanan, T. Killeen, Z. Lin, N. Gimelshein, L. Antiga, A. Desmaison, A. Köpf, E. Yang, Z. DeVito, M. Raison, A. Tejani, S. Chilamkurthy, B. Steiner, L. Fang, J. Bai, and S. Chintala, PyTorch: An Imperative Style, High-Performance Deep Learning Library (2019), arXiv:1912.01703.

[40] P. Moritz, R. Nishihara, S. Wang, A. Tumanov, R. Liaw, E. Liang, M. Elibol, Z. Yang, W. Paul, M. I. Jordan, and I. Stoica, Ray: A Distributed Framework for Emerging AI Applications (2018), arXiv:1712.05889.

[41] X. Chen, C. Liang, D. Huang, E. Real, K. Wang, Y. Liu, H. Pham, X. Dong, T. Luong, C.-J. Hsieh, Y. Lu, and Q. V. Le, Symbolic Discovery of Optimization Algorithms (2023), arXiv:2302.06675.

[42] U. Ellwanger, C. Hugonie, and A. M. Teixeira, The Next-to-Minimal Supersymmetric Standard Model, *Phys. Rept.* **496**, 1 (2010).

[43] T. Robens, T. Stefaniak, and J. Wittbrodt, Two-real-scalar-singlet extension of the SM: LHC phenomenology and benchmark scenarios, *Eur. Phys. J. C* **80**, 151 (2020).

[44] H. Abouabid, A. Arhrib, D. Azevedo, J. E. Falaki, P. M. Ferreira, M. Mühlleitner, and R. Santos, Benchmarking di-Higgs production in various extended Higgs sector models, *J. High Energy Phys.* **09**, 011.

[45] G. Aad et al. (ATLAS Collaboration), Search for a resonance decaying into a scalar particle and a Higgs boson in the final state with two bottom quarks and two photons in proton–proton collisions at  $\sqrt{s} = 13$  TeV with the ATLAS detector, *J. High Energy Phys.* **11**, 047.

[46] A. Hayrapetyan et al. (CMS Collaboration), Search for a new scalar resonance decaying to a Higgs boson and another new scalar particle in the final state with two bottom quarks and two photons in proton–proton collisions at  $\sqrt{s} = 13$  TeV, *J. High Energy Phys.* **12**, 178.

[47] A. Tumasyan et al. (CMS Collaboration), Search for a heavy Higgs boson decaying into two lighter Higgs bosons in the  $\tau\tau bb$  final state at 13 TeV, *J. High Energy Phys.* **11**, 057.

[48] A. Tumasyan et al. (CMS Collaboration), Search for a massive scalar resonance decaying to a light scalar and a Higgs boson in the four b quarks final state with boosted topology, *Phys. Lett. B* **842**, 137392 (2023).

[49] CERN Open Data, CERN Open Data Policy for the LHC Experiments (2020), CERN Open Data Portal.

[50] CERN Open Data, CERN Open Data Portal (2021), accessed via CERN Open Data.

[51] CERN Open Data, CERN Open Data Privacy Policy (2021), CERN Open Data Portal.

[52] CMS Collaboration, 2020 CMS Data Preservation, Reuse and Open Access Policy (2020), CMS Open Data.

[53] CMS Collaboration, CMS Open Data: NMSSM  $X \rightarrow YH \rightarrow 2b2W$  Signal Samples, <https://opendata.cern.ch> (2024), dataset-specific DOIs for all mass points used in the NMSSM  $X \rightarrow YH \rightarrow 2b2W$  grid study are listed in Appendix A.

[54] S. Chatrchyan *et al.* (CMS Collaboration), The CMS Experiment at the CERN LHC, *JINST* **3**, S08004.

[55] CMS Collaboration, Simulated dataset TTTToSemiLeptonic\_TuneCP5\_13TeV-powheg-pythia8 in NANOAODSIM format for 2016 collision data., CERN Open Data Portal (2024).

[56] CMS Collaboration, Simulated dataset DYBJetsToLL\_M-50\_Zpt-100to200\_TuneCP5\_13TeV-madgraphMLM-pythia8 in NANOAODSIM format for 2016 collision data., CERN Open Data Portal (2024).

[57] CMS Collaboration, Simulated dataset DYBJetsToLL\_M-50\_Zpt-200toInf\_TuneCP5\_13TeV-madgraphMLM-pythia8 in NANOAODSIM format for 2016 collision data., CERN Open Data Portal (2024).

[58] CMS Collaboration, Simulated dataset ST\_s-channel\_4f\_leptonDecays\_TuneCP5\_13TeV-amcatnlo-pythia8 in NANOAODSIM format for 2016 collision data., CERN Open Data Portal (2024).

[59] CMS Collaboration, Simulated dataset ST\_t-channel\_top\_4f\_InclusiveDecays\_TuneCP5CR1\_13TeV-powheg-madspin-pythia8 in NANOAODSIM format for 2016 collision data., CERN Open Data Portal (2024).

[60] CMS Collaboration, Simulated dataset ST\_t-channel\_antitop\_4f\_InclusiveDecays\_TuneCP5\_13TeV-powheg-madspin-pythia8 in NANOAODSIM format for 2016 collision data., CERN Open Data Portal (2024).

[61] CMS Collaboration, Simulated dataset ST\_tW\_top\_5f\_inclusiveDecays\_TuneCP5\_13TeV-powheg-pythia8 in NANOAODSIM format for 2016 collision data., CERN Open Data Portal (2024).

[62] CMS Collaboration, Simulated dataset ST\_tW\_antitop\_5f\_inclusiveDecays\_TuneCP5\_13TeV-powheg-pythia8 in NANOAODSIM format for 2016 collision data., CERN Open Data Portal (2024).

[63] T. Chen and C. Guestrin, XGBoost: A scalable tree boosting system, in Proceedings of the 22nd ACM SIGKDD International Conference on Knowledge Discovery and Data Mining (ACM, New York, NY, USA, 2016) pp. 785–794.

[64] N. Hollmann, S. Müller, L. Purucker, A. Krishnakumar, M. Körfer, S. B. Hoo, R. T. Schirrmeister, and F. Hutter, Accurate predictions on small data with a tabular foundation model, *Nature* **637**, 319 (2025).

[65] L. Grinsztajn, K. Flöge, O. Key, F. Birkel, P. Jund, B. Roof, B. Jäger, D. Safaric, S. Alessi, A. Hayler, M. Maimun, R. Yu, F. Jablonski, S. B. Hoo, A. Garg, J. Robertson, M. Bühler, V. Moroshan, L. Purucker, C. Cornu, L. C. Wehrhahn, A. Bonetto, B. Schölkopf, S. Gambhir, N. Hollmann, and F. Hutter, TabPFN-2.5: Advancing the State of the Art in Tabular Foundation Models (2025), arXiv:2511.08667.

[66] N. Houlsby, A. Giurgiu, S. Jastrzebski, B. Morrone, Q. d. Laroussilhe, A. Gesmundo, M. Attariyan, and S. Gelly, Parameter-Efficient Transfer Learning for NLP (2019), arXiv:1902.00751.

[67] K. Black, J. Gallicchio, J. Huth, M. Kagan, M. D. Schwartz, and B. Tweedie, Multivariate discrimination and the Higgs + W/Z search, *J. High Energy Phys.* **2011** (4), 69.

[68] G. Aad *et al.* (ATLAS Collaboration), A detailed map of Higgs boson interactions by the ATLAS experiment ten years after the discovery, *Nature* **607**, 52 (2022), [Erratum: *Nature* 612, E24 (2022)].

[69] M. Cepeda, S. Gori, V. I. Martinez Outschoorn, and J. Shelton, Exotic higgs decays, *Annual Review of Nuclear and Particle Science* **72**, 119 (2022).

[70] C.-W. Chiang, F.-Y. Hsieh, S.-C. Hsu, and I. Low, Deep learning to improve the sensitivity of Di-Higgs searches in the 4b channel, *J. High Energy Phys.* **09**, 139.

[71] ATLAS Collaboration, Search for decays of the higgs boson into scalar particles decaying into four or six  $b$  quarks using  $pp$  collisions at  $\sqrt{s} = 13$  TeV with the ATLAS detector, *Phys. Rev. D* **112**, 072005 (2025).

[72] CMS collaboration, Search for the decay of the Higgs boson to a pair of light pseudoscalar bosons in the final state with four bottom quarks in proton-proton collisions at  $\sqrt{s} = 13$  TeV, *J. High Energy Phys.* **2024** (6), 97.

[73] ATLAS Collaboration, Search for a new pseudoscalar decaying into a pair of bottom and antibottom quarks in top-associated production in  $\sqrt{s} = 13$  TeV proton–proton collisions with the ATLAS detector, *Eur. Phys. J. C* **85**, 886 (2025).

[74] Y. Afik and J. R. M. d. Nova, Entanglement and quantum tomography with top quarks at the LHC, *Eur. Phys. J. Plus* **136**, 907 (2025).

[75] Y. Afik and J. R. M. d. Nova, Quantum information with top quarks in QCD, *Quantum* **6**, 820 (2022).

[76] ATLAS Collaboration, Observation of quantum entanglement in top-quark pairs using the ATLAS detector, *Nature* **633**, 542 (2024).

[77] CMS Collaboration, Observation of quantum entanglement in top quark pair production in proton–proton collisions at  $\sqrt{s} = 13$  TeV, *Rept. Prog. Phys.* **87**, 117801 (2024).

[78] Ü. Fano, Pairs of two-level systems, *Rev. Mod. Phys.* **55**, 855 (1983).

[79] C. Severi, C. D. E. Boschi, F. Maltoni, and M. Sioli, Quantum tops at the LHC: from entanglement to Bell inequalities, *Eur. Phys. J. C* **82**, 285 (2022).

[80] G. Aad *et al.* (ATLAS Collaboration), Luminosity determination in  $pp$  collisions at  $\sqrt{s} = 13$  TeV using the ATLAS detector at the LHC, *Eur. Phys. J. C* **83**, 982 (2023).

[81] A. Hallin, J. Isaacson, G. Kasieczka, C. Krause, B. Nachman, T. Quadfasel, M. Schlaffer, D. Shih, and M. Sommerhalder, Classifying anomalies through outer density estimation, *Phys. Rev. D* **106**, 055006 (2022).

[82] C. Cesarotti, Y. Soreq, M. J. Strassler, J. Thaler, and W. Xue, Searching in CMS Open Data for Dimuon Resonances with Substantial Transverse Momentum, *Phys. Rev. D* **100**, 015021 (2019).

[83] A. Hayrapetyan *et al.* (CMS Collaboration), Search for direct production of GeV-scale resonances decaying to a pair of muons in proton-proton collisions at  $\sqrt{s} = 13$  TeV, *J. High Energy Phys.* **12**, 070.

[84] W. Bhimji, P. Calafuria, R. Chakkappai, P.-W. Chang, Y.-T. Chou, S. Diefenbacher, J. Dudley, S. Farrell, A. Ghosh, I. Guyon, C. Harris, S.-C. Hsu, E. E. Khoda,

R. Lyscar, A. Michon, B. Nachman, P. Nugent, M. Reymond, D. Rousseau, B. Sluijter, B. Thorne, I. Ullah, and

Y. Zhang, FAIR Universe HiggsML Uncertainty Challenge Competition (2024), arXiv:2410.02867.

## Appendix A: Complete List of CMS Open Data NMSSM Datasets

Table V: CMS Open Data simulated NMSSM signal datasets used in the grid study, corresponding to the process  $X \rightarrow Y H_{SM} \rightarrow 2b, 2W \rightarrow 2b, 2q, \ell\nu$ . This table lists mass points with  $M_X = 240\text{--}500$  GeV, together with the corresponding  $M_Y$  values and dataset-specific DOI links.

$M_X$ [GeV]	$M_Y$ [GeV]	Full DOI Link
240	60	<a href="https://doi.org/10.7483/OPENDATA.CMS.42E8.PJND">https://doi.org/10.7483/OPENDATA.CMS.42E8.PJND</a>
	70	<a href="https://doi.org/10.7483/OPENDATA.CMS.N8C4.0GEQ">https://doi.org/10.7483/OPENDATA.CMS.N8C4.0GEQ</a>
	80	<a href="https://doi.org/10.7483/OPENDATA.CMS.JBDY.Q45P">https://doi.org/10.7483/OPENDATA.CMS.JBDY.Q45P</a>
	90	<a href="https://doi.org/10.7483/OPENDATA.CMS.AGCH.S6H4">https://doi.org/10.7483/OPENDATA.CMS.AGCH.S6H4</a>
	100	<a href="https://doi.org/10.7483/OPENDATA.CMS.AA8A.WV8">https://doi.org/10.7483/OPENDATA.CMS.AA8A.WV8</a>
280	60	<a href="https://doi.org/10.7483/OPENDATA.CMS.GGVL.V3RG">https://doi.org/10.7483/OPENDATA.CMS.GGVL.V3RG</a>
	70	<a href="https://doi.org/10.7483/OPENDATA.CMS.HL6H.V95D">https://doi.org/10.7483/OPENDATA.CMS.HL6H.V95D</a>
	80	<a href="https://doi.org/10.7483/OPENDATA.CMS.TFP1.8U4M">https://doi.org/10.7483/OPENDATA.CMS.TFP1.8U4M</a>
	90	<a href="https://doi.org/10.7483/OPENDATA.CMS.08Q8.31AB">https://doi.org/10.7483/OPENDATA.CMS.08Q8.31AB</a>
	100	<a href="https://doi.org/10.7483/OPENDATA.CMS.9EE5.NH12">https://doi.org/10.7483/OPENDATA.CMS.9EE5.NH12</a>
	125	<a href="https://doi.org/10.7483/OPENDATA.CMS.5NCN.YPQG">https://doi.org/10.7483/OPENDATA.CMS.5NCN.YPQG</a>
	150	<a href="https://doi.org/10.7483/OPENDATA.CMS.EDMW.5KMO">https://doi.org/10.7483/OPENDATA.CMS.EDMW.5KMO</a>
300	60	<a href="https://doi.org/10.7483/OPENDATA.CMS.OE6Z.PMSJ">https://doi.org/10.7483/OPENDATA.CMS.OE6Z.PMSJ</a>
	70	<a href="https://doi.org/10.7483/OPENDATA.CMS.BFP0.PWA2">https://doi.org/10.7483/OPENDATA.CMS.BFP0.PWA2</a>
	80	<a href="https://doi.org/10.7483/OPENDATA.CMS.5DYZ.XY30">https://doi.org/10.7483/OPENDATA.CMS.5DYZ.XY30</a>
	90	<a href="https://doi.org/10.7483/OPENDATA.CMS.1BFE.PRHF">https://doi.org/10.7483/OPENDATA.CMS.1BFE.PRHF</a>
	100	<a href="https://doi.org/10.7483/OPENDATA.CMS.L8RX.J05H">https://doi.org/10.7483/OPENDATA.CMS.L8RX.J05H</a>
	125	<a href="https://doi.org/10.7483/OPENDATA.CMS.531U.IN34">https://doi.org/10.7483/OPENDATA.CMS.531U.IN34</a>
320	60	<a href="https://doi.org/10.7483/OPENDATA.CMS.QS15.X00H">https://doi.org/10.7483/OPENDATA.CMS.QS15.X00H</a>
	70	<a href="https://doi.org/10.7483/OPENDATA.CMS.941S.93RX">https://doi.org/10.7483/OPENDATA.CMS.941S.93RX</a>
	80	<a href="https://doi.org/10.7483/OPENDATA.CMS.0QFT.IQSH">https://doi.org/10.7483/OPENDATA.CMS.0QFT.IQSH</a>
	90	<a href="https://doi.org/10.7483/OPENDATA.CMS.5ID5.WVOE">https://doi.org/10.7483/OPENDATA.CMS.5ID5.WVOE</a>
	100	<a href="https://doi.org/10.7483/OPENDATA.CMS.X7AI.D6ZQ">https://doi.org/10.7483/OPENDATA.CMS.X7AI.D6ZQ</a>
	125	<a href="https://doi.org/10.7483/OPENDATA.CMS.N93P.RNJ8">https://doi.org/10.7483/OPENDATA.CMS.N93P.RNJ8</a>
360	60	<a href="https://doi.org/10.7483/OPENDATA.CMS.P1T2.1P2V">https://doi.org/10.7483/OPENDATA.CMS.P1T2.1P2V</a>
	70	<a href="https://doi.org/10.7483/OPENDATA.CMS.U3ET.OENN">https://doi.org/10.7483/OPENDATA.CMS.U3ET.OENN</a>
	80	<a href="https://doi.org/10.7483/OPENDATA.CMS.7J45.M2W4">https://doi.org/10.7483/OPENDATA.CMS.7J45.M2W4</a>
	125	<a href="https://doi.org/10.7483/OPENDATA.CMS.CE37.C5T1">https://doi.org/10.7483/OPENDATA.CMS.CE37.C5T1</a>
400	60	<a href="https://doi.org/10.7483/OPENDATA.CMS.DBJF.V6HO">https://doi.org/10.7483/OPENDATA.CMS.DBJF.V6HO</a>
	80	<a href="https://doi.org/10.7483/OPENDATA.CMS.YLOT.TYTR">https://doi.org/10.7483/OPENDATA.CMS.YLOT.TYTR</a>
	90	<a href="https://doi.org/10.7483/OPENDATA.CMS.XXXN.36KA">https://doi.org/10.7483/OPENDATA.CMS.XXXN.36KA</a>
	100	<a href="https://doi.org/10.7483/OPENDATA.CMS.ALBO.KFDA">https://doi.org/10.7483/OPENDATA.CMS.ALBO.KFDA</a>
	150	<a href="https://doi.org/10.7483/OPENDATA.CMS.V1GT.7XXP">https://doi.org/10.7483/OPENDATA.CMS.V1GT.7XXP</a>
	250	<a href="https://doi.org/10.7483/OPENDATA.CMS.K8P0.4TMK">https://doi.org/10.7483/OPENDATA.CMS.K8P0.4TMK</a>
500	60	<a href="https://doi.org/10.7483/OPENDATA.CMS.2Z9V.5ZYV">https://doi.org/10.7483/OPENDATA.CMS.2Z9V.5ZYV</a>
	70	<a href="https://doi.org/10.7483/OPENDATA.CMS.PW1Y.U031">https://doi.org/10.7483/OPENDATA.CMS.PW1Y.U031</a>
	80	<a href="https://doi.org/10.7483/OPENDATA.CMS.QYTR.VLWZ">https://doi.org/10.7483/OPENDATA.CMS.QYTR.VLWZ</a>
	90	<a href="https://doi.org/10.7483/OPENDATA.CMS.JP5A.5DGC">https://doi.org/10.7483/OPENDATA.CMS.JP5A.5DGC</a>
	100	<a href="https://doi.org/10.7483/OPENDATA.CMS.1RVY.MTUJ">https://doi.org/10.7483/OPENDATA.CMS.1RVY.MTUJ</a>
	125	<a href="https://doi.org/10.7483/OPENDATA.CMS.RBC8.ETKI">https://doi.org/10.7483/OPENDATA.CMS.RBC8.ETKI</a>
	150	<a href="https://doi.org/10.7483/OPENDATA.CMS.SP43.1Z2H">https://doi.org/10.7483/OPENDATA.CMS.SP43.1Z2H</a>
	250	<a href="https://doi.org/10.7483/OPENDATA.CMS.3ITI.81B8">https://doi.org/10.7483/OPENDATA.CMS.3ITI.81B8</a>
	300	<a href="https://doi.org/10.7483/OPENDATA.CMS.FCGQ.3IRJ">https://doi.org/10.7483/OPENDATA.CMS.FCGQ.3IRJ</a>

Table VI: CMS Open Data simulated NMSSM signal datasets used in the grid study ( $M_X = 600\text{--}900$  GeV).

$M_X$ [GeV]	$M_Y$ [GeV]	Full DOI Link
600	60	<a href="https://doi.org/10.7483/OPENDATA.CMS.HFxD.GI5F">https://doi.org/10.7483/OPENDATA.CMS.HFxD.GI5F</a>
	70	<a href="https://doi.org/10.7483/OPENDATA.CMS.UC52.33F0">https://doi.org/10.7483/OPENDATA.CMS.UC52.33F0</a>
	80	<a href="https://doi.org/10.7483/OPENDATA.CMS.J6UR.QL33">https://doi.org/10.7483/OPENDATA.CMS.J6UR.QL33</a>
	90	<a href="https://doi.org/10.7483/OPENDATA.CMS.38F8.MDB4">https://doi.org/10.7483/OPENDATA.CMS.38F8.MDB4</a>
	100	<a href="https://doi.org/10.7483/OPENDATA.CMS.8L2I.Q6TW">https://doi.org/10.7483/OPENDATA.CMS.8L2I.Q6TW</a>
	125	<a href="https://doi.org/10.7483/OPENDATA.CMS.JKUE.1Q88">https://doi.org/10.7483/OPENDATA.CMS.JKUE.1Q88</a>
	150	<a href="https://doi.org/10.7483/OPENDATA.CMS.P4UV.P7FB">https://doi.org/10.7483/OPENDATA.CMS.P4UV.P7FB</a>
	250	<a href="https://doi.org/10.7483/OPENDATA.CMS.C1FI.C49L">https://doi.org/10.7483/OPENDATA.CMS.C1FI.C49L</a>
	300	<a href="https://doi.org/10.7483/OPENDATA.CMS.SU7D.U5UY">https://doi.org/10.7483/OPENDATA.CMS.SU7D.U5UY</a>
	400	<a href="https://doi.org/10.7483/OPENDATA.CMS.TIDO.GN9S">https://doi.org/10.7483/OPENDATA.CMS.TIDO.GN9S</a>
650	60	<a href="https://doi.org/10.7483/OPENDATA.CMS.EZ30.AV2E">https://doi.org/10.7483/OPENDATA.CMS.EZ30.AV2E</a>
	70	<a href="https://doi.org/10.7483/OPENDATA.CMS.HCST.DUYS">https://doi.org/10.7483/OPENDATA.CMS.HCST.DUYS</a>
	80	<a href="https://doi.org/10.7483/OPENDATA.CMS.AWYC.A1TT">https://doi.org/10.7483/OPENDATA.CMS.AWYC.A1TT</a>
	90	<a href="https://doi.org/10.7483/OPENDATA.CMS.OD7R.RIUI">https://doi.org/10.7483/OPENDATA.CMS.OD7R.RIUI</a>
	100	<a href="https://doi.org/10.7483/OPENDATA.CMS.9G3N.F5D8">https://doi.org/10.7483/OPENDATA.CMS.9G3N.F5D8</a>
	125	<a href="https://doi.org/10.7483/OPENDATA.CMS.46FL.3KLH">https://doi.org/10.7483/OPENDATA.CMS.46FL.3KLH</a>
	150	<a href="https://doi.org/10.7483/OPENDATA.CMS.299I.UMT7">https://doi.org/10.7483/OPENDATA.CMS.299I.UMT7</a>
	190	<a href="https://doi.org/10.7483/OPENDATA.CMS.I7JG.03IJ">https://doi.org/10.7483/OPENDATA.CMS.I7JG.03IJ</a>
	250	<a href="https://doi.org/10.7483/OPENDATA.CMS.IVU7.2GW4">https://doi.org/10.7483/OPENDATA.CMS.IVU7.2GW4</a>
	300	<a href="https://doi.org/10.7483/OPENDATA.CMS.0000.V4QJ">https://doi.org/10.7483/OPENDATA.CMS.0000.V4QJ</a>
	350	<a href="https://doi.org/10.7483/OPENDATA.CMS.FL1K.YVYR">https://doi.org/10.7483/OPENDATA.CMS.FL1K.YVYR</a>
	400	<a href="https://doi.org/10.7483/OPENDATA.CMS.DOBH.4990">https://doi.org/10.7483/OPENDATA.CMS.DOBH.4990</a>
	450	<a href="https://doi.org/10.7483/OPENDATA.CMS.L90F.NLRL">https://doi.org/10.7483/OPENDATA.CMS.L90F.NLRL</a>
	500	<a href="https://doi.org/10.7483/OPENDATA.CMS.EAWX.CCIT">https://doi.org/10.7483/OPENDATA.CMS.EAWX.CCIT</a>
700	60	<a href="https://doi.org/10.7483/OPENDATA.CMS.41S7.GCTT">https://doi.org/10.7483/OPENDATA.CMS.41S7.GCTT</a>
	70	<a href="https://doi.org/10.7483/OPENDATA.CMS.FPE4.HIFB">https://doi.org/10.7483/OPENDATA.CMS.FPE4.HIFB</a>
	80	<a href="https://doi.org/10.7483/OPENDATA.CMS.WE9R.FOAU">https://doi.org/10.7483/OPENDATA.CMS.WE9R.FOAU</a>
	90	<a href="https://doi.org/10.7483/OPENDATA.CMS.64R7.87DK">https://doi.org/10.7483/OPENDATA.CMS.64R7.87DK</a>
	100	<a href="https://doi.org/10.7483/OPENDATA.CMS.VCSM.TM82">https://doi.org/10.7483/OPENDATA.CMS.VCSM.TM82</a>
	125	<a href="https://doi.org/10.7483/OPENDATA.CMS.Q27T.DMI4">https://doi.org/10.7483/OPENDATA.CMS.Q27T.DMI4</a>
	150	<a href="https://doi.org/10.7483/OPENDATA.CMS.EW50.7C6V">https://doi.org/10.7483/OPENDATA.CMS.EW50.7C6V</a>
	250	<a href="https://doi.org/10.7483/OPENDATA.CMS.E3IY.UIBA">https://doi.org/10.7483/OPENDATA.CMS.E3IY.UIBA</a>
	300	<a href="https://doi.org/10.7483/OPENDATA.CMS.J06H.J5GG">https://doi.org/10.7483/OPENDATA.CMS.J06H.J5GG</a>
	400	<a href="https://doi.org/10.7483/OPENDATA.CMS.2M2W.FJ0I">https://doi.org/10.7483/OPENDATA.CMS.2M2W.FJ0I</a>
	500	<a href="https://doi.org/10.7483/OPENDATA.CMS.RT9R.Q5H3">https://doi.org/10.7483/OPENDATA.CMS.RT9R.Q5H3</a>
800	60	<a href="https://doi.org/10.7483/OPENDATA.CMS.RX5B.0RF6">https://doi.org/10.7483/OPENDATA.CMS.RX5B.0RF6</a>
	70	<a href="https://doi.org/10.7483/OPENDATA.CMS.LHI3.4Q0D">https://doi.org/10.7483/OPENDATA.CMS.LHI3.4Q0D</a>
	80	<a href="https://doi.org/10.7483/OPENDATA.CMS.7RAL.Y2GM">https://doi.org/10.7483/OPENDATA.CMS.7RAL.Y2GM</a>
	90	<a href="https://doi.org/10.7483/OPENDATA.CMS.37F6.Q1RV">https://doi.org/10.7483/OPENDATA.CMS.37F6.Q1RV</a>
	100	<a href="https://doi.org/10.7483/OPENDATA.CMS.C1ZA.HK5D">https://doi.org/10.7483/OPENDATA.CMS.C1ZA.HK5D</a>
	125	<a href="https://doi.org/10.7483/OPENDATA.CMS.D9I9.77TL">https://doi.org/10.7483/OPENDATA.CMS.D9I9.77TL</a>
	250	<a href="https://doi.org/10.7483/OPENDATA.CMS.RWOG.KG9V">https://doi.org/10.7483/OPENDATA.CMS.RWOG.KG9V</a>
	300	<a href="https://doi.org/10.7483/OPENDATA.CMS.NY9X.AHV9">https://doi.org/10.7483/OPENDATA.CMS.NY9X.AHV9</a>
	400	<a href="https://doi.org/10.7483/OPENDATA.CMS.ZJRA.9LJN">https://doi.org/10.7483/OPENDATA.CMS.ZJRA.9LJN</a>
	500	<a href="https://doi.org/10.7483/OPENDATA.CMS.7235.F1D9">https://doi.org/10.7483/OPENDATA.CMS.7235.F1D9</a>
900	60	<a href="https://doi.org/10.7483/OPENDATA.CMS.4TJA.25NZ">https://doi.org/10.7483/OPENDATA.CMS.4TJA.25NZ</a>
	70	<a href="https://doi.org/10.7483/OPENDATA.CMS.UMW3.4R3Z">https://doi.org/10.7483/OPENDATA.CMS.UMW3.4R3Z</a>
	80	<a href="https://doi.org/10.7483/OPENDATA.CMS.EPY7.K8J3">https://doi.org/10.7483/OPENDATA.CMS.EPY7.K8J3</a>
	90	<a href="https://doi.org/10.7483/OPENDATA.CMS.ECNI.D3KU">https://doi.org/10.7483/OPENDATA.CMS.ECNI.D3KU</a>
	100	<a href="https://doi.org/10.7483/OPENDATA.CMS.Q02V.WK9J">https://doi.org/10.7483/OPENDATA.CMS.Q02V.WK9J</a>
	125	<a href="https://doi.org/10.7483/OPENDATA.CMS.GFZ4.VX65">https://doi.org/10.7483/OPENDATA.CMS.GFZ4.VX65</a>
	150	<a href="https://doi.org/10.7483/OPENDATA.CMS.NWIS.HLEQ">https://doi.org/10.7483/OPENDATA.CMS.NWIS.HLEQ</a>
	250	<a href="https://doi.org/10.7483/OPENDATA.CMS.CIAN.24AI">https://doi.org/10.7483/OPENDATA.CMS.CIAN.24AI</a>
	300	<a href="https://doi.org/10.7483/OPENDATA.CMS.F28L.1GDG">https://doi.org/10.7483/OPENDATA.CMS.F28L.1GDG</a>
	400	<a href="https://doi.org/10.7483/OPENDATA.CMS.FI4Z.X28Z">https://doi.org/10.7483/OPENDATA.CMS.FI4Z.X28Z</a>
500	500	<a href="https://doi.org/10.7483/OPENDATA.CMS.OWJE.9911">https://doi.org/10.7483/OPENDATA.CMS.OWJE.9911</a>
	600	<a href="https://doi.org/10.7483/OPENDATA.CMS.81IV.4C6W">https://doi.org/10.7483/OPENDATA.CMS.81IV.4C6W</a>
700	700	<a href="https://doi.org/10.7483/OPENDATA.CMS.VKOC.PPFM">https://doi.org/10.7483/OPENDATA.CMS.VKOC.PPFM</a>

Table VII: CMS Open Data simulated NMSSM signal datasets used in the grid study ( $M_X = 1000$  GeV).

$M_X$ [GeV]	$M_Y$ [GeV]	Full DOI Link
1000	60	<a href="https://doi.org/10.7483/OPENDATA.CMS.5A6N.SAJA">https://doi.org/10.7483/OPENDATA.CMS.5A6N.SAJA</a>
	70	<a href="https://doi.org/10.7483/OPENDATA.CMS.ZR27.TMIP">https://doi.org/10.7483/OPENDATA.CMS.ZR27.TMIP</a>
	80	<a href="https://doi.org/10.7483/OPENDATA.CMS.OZFH.7PXA">https://doi.org/10.7483/OPENDATA.CMS.OZFH.7PXA</a>
	90	<a href="https://doi.org/10.7483/OPENDATA.CMS.TNHW.Z68A">https://doi.org/10.7483/OPENDATA.CMS.TNHW.Z68A</a>
	100	<a href="https://doi.org/10.7483/OPENDATA.CMS.I4ZE.1J60">https://doi.org/10.7483/OPENDATA.CMS.I4ZE.1J60</a>
	125	<a href="https://doi.org/10.7483/OPENDATA.CMS.VJXV.24QV">https://doi.org/10.7483/OPENDATA.CMS.VJXV.24QV</a>
	150	<a href="https://doi.org/10.7483/OPENDATA.CMS.7WP9.7H4L">https://doi.org/10.7483/OPENDATA.CMS.7WP9.7H4L</a>
	190	<a href="https://doi.org/10.7483/OPENDATA.CMS.4ZZJ.02C1">https://doi.org/10.7483/OPENDATA.CMS.4ZZJ.02C1</a>
	250	<a href="https://doi.org/10.7483/OPENDATA.CMS.69F2.RNLU">https://doi.org/10.7483/OPENDATA.CMS.69F2.RNLU</a>
	300	<a href="https://doi.org/10.7483/OPENDATA.CMS.G1M9.75WJ">https://doi.org/10.7483/OPENDATA.CMS.G1M9.75WJ</a>
	350	<a href="https://doi.org/10.7483/OPENDATA.CMS.NS38.A7KQ">https://doi.org/10.7483/OPENDATA.CMS.NS38.A7KQ</a>
	400	<a href="https://doi.org/10.7483/OPENDATA.CMS.WCNV.Q903">https://doi.org/10.7483/OPENDATA.CMS.WCNV.Q903</a>
	450	<a href="https://doi.org/10.7483/OPENDATA.CMS.XL80.EWG5">https://doi.org/10.7483/OPENDATA.CMS.XL80.EWG5</a>
	500	<a href="https://doi.org/10.7483/OPENDATA.CMS.Q3X2.182W">https://doi.org/10.7483/OPENDATA.CMS.Q3X2.182W</a>
	600	<a href="https://doi.org/10.7483/OPENDATA.CMS.4TZY.YZUL">https://doi.org/10.7483/OPENDATA.CMS.4TZY.YZUL</a>
	700	<a href="https://doi.org/10.7483/OPENDATA.CMS.72RL.UOB2">https://doi.org/10.7483/OPENDATA.CMS.72RL.UOB2</a>
	800	<a href="https://doi.org/10.7483/OPENDATA.CMS.0GUO.0Y8V">https://doi.org/10.7483/OPENDATA.CMS.0GUO.0Y8V</a>